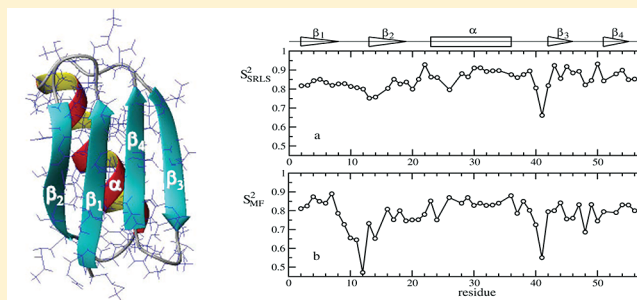


# Slowly Relaxing Local Structure (SRLS) Analysis of $^{15}\text{N}$ -H Relaxation from the Prototypical Small Proteins GB1 and GB3

Yury E. Shapiro\* and Eva Meirovitch\*

The Mina and Everard Goodman Faculty of Life Sciences, Bar-Ilan University, Ramat-Gan 52900 Israel

**ABSTRACT:**  $^{15}\text{N}$ -H relaxation parameters from the first (GB1) and third (GB3) immunoglobulin-binding domains of streptococcal protein G were analyzed previously with the traditional model-free (MF) method. These proteins comprise an  $\alpha$ -helix and a four-stranded  $\beta$ -sheet. An extensive study of GB1 (GB3) used combined three-field (five-field) data acquired in the 278–323 K range (at 297 K). For successful analysis of the GB3 data, it was necessary to allow for variations in the  $^{15}\text{N}$  chemical shift anisotropy (CSA) tensor and virtually eliminate the local motion. In the case of GB1, the spectral density was parametrized. Here, we analyze these data with the slowly relaxing local structure (SRLS) approach, which is the generalization of MF in allowing for general tensorial properties, and accounting for mode-coupling. A standard (featuring constant magnetic tensors) SRLS fitting scheme is used. This analysis accounts for the important asymmetry of the local spatial restrictions; it provides physical order parameters, local diffusion rates, related activation energies, and key features of local geometry. Using data from GB3 we show that the main local ordering axis is  $C_{i-1}^{\alpha} - C_i^{\alpha}$ , and the average axial (rhombic) order parameter is  $-0.457 \pm 0.017$  ( $1.156 \pm 0.015$ ) for the  $\alpha$ -helix and  $-0.484 \pm 0.002$  ( $1.10 \pm 0.04$ ) for the rest of the polypeptide chain. The N-H bonds within (outside of) the  $\alpha$ -helix reorient locally with an average correlation time,  $\langle\tau\rangle$ , of 310 (130) ps, as compared to 3.33 ns for the global tumbling. Several N-H bonds in the loops  $\beta_1/\beta_2$ ,  $\beta_2/\alpha$ -helix, and  $\alpha$ -helix/ $\beta_3$  have  $\langle\tau\rangle$  of 380, 320, and 750 ps, respectively. The distinctive experimental data of the  $\alpha$ -helix are due to relatively weak and substantially rhombic local ordering and slow local motion. For GB1, we derive activation energies from local diffusion rates. They are  $43.3 \pm 7.1$  kJ/mol for the  $\beta$ -strands,  $24.7 \pm 3.9$  kJ/mol for the  $\alpha$ -helix (and approximately for the loop  $\beta_3/\beta_4$ ), and  $18.9 \pm 1.8$  kJ/mol for the other loops. The physical SRLS description provides new insights into the backbone dynamics of GB1 and GB3 in particular, and proteins in general.



## 1. INTRODUCTION

The first (GB1) and third (GB3) immunoglobulin-binding domains of streptococcal protein G are unusually stable 56-residue proteins with no complicated features superimposed on the intrinsic properties of the polypeptide chain.<sup>1–3</sup> The sequences of GB1 and GB3 include 17 types of amino acids; they differ by seven residues. The similar tertiary structures of these proteins consist of a  $\alpha$ -helix (residues 23–36) packed against a four-stranded antiparallel–parallel–antiparallel  $\beta$ -sheet comprising the strands denoted  $\beta_1$  to  $\beta_4$  (residues 2–8, 13–19, 42–46, and 51–55) and the hairpin turns  $\beta_1/\beta_2$  and  $\beta_3/\beta_4$  (residues 9–12 and 47–50). A schematic representation of GB3 is shown in Figure 1.

GB3 is among the first proteins for which a good structural model was obtained using solely the solid-state NMR chemical shifts as input to the Chemical-Shift-Rosetta protocol.<sup>5</sup> The crystal structure of GB3 was determined at 1.1 Å resolution (PDB code 1IGD).<sup>1</sup> It was refined using  $^1\text{D}_{\text{NH}}$  and  $^1\text{D}_{\text{CaHa}}$  residual dipolar couplings (RDCs) to the structure with PDB code 2OED.<sup>2</sup> The solution structure of GB1 was determined in early work.<sup>3</sup> An RDC-based study focusing on backbone proton position and dynamics was carried out for GB3.<sup>6</sup> On the basis of molecular dynamics (MD) simulations, it was shown for GB3 that a two-state ensemble represents the simplest equilibrium

description of anisotropic motion consistent with RDCs, B-factors, and  $^{15}\text{N}$  relaxation analysis.<sup>7</sup> 1.1  $\mu\text{s}$  long MD simulations support fast anisotropic backbone motions in GB3.<sup>8</sup>

$^{15}\text{N}$ -H spin relaxation was also studied.<sup>9–13</sup> Of particular interest to the present work are refs 9 and 10 on GB3, and ref 13 on GB1. These studies analyzed extensive experimental data sets in the context of the model-free (MF)<sup>14–16</sup> method. In describing  $^{15}\text{N}$ -H relaxation one has to account for the global tumbling of the protein and the local motion of the N-H bond. MF assumes that these motions are decoupled due to large time scale separation between their rates.<sup>14–16</sup> In addition, it assumes (implicitly) that the tensorial properties of the local motion and the local ordering, as well as the local geometry, are simple. Because the MF spectral densities (which underlie the expressions for the experimentally measured relaxation parameters) are simple, data-fitting is often successful statistically, although not necessarily appropriate physically, when limited data sets are used. In the case of extensive data sets, the statistical requirements are typically not fulfilled when standard MF is used.

Received: January 9, 2012

Revised: March 4, 2012

Published: March 7, 2012

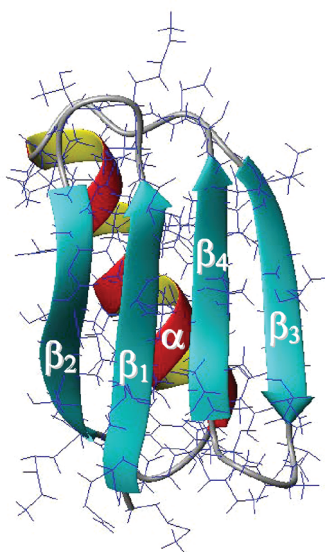


**Figure 1.** Ribbon diagram of the GB3 backbone together with a sketchy representation of the side-chains generated using the PDB structure 2OED and the program MolMol.<sup>†</sup>

We applied in recent years the slowly relaxing local structure (SRLS) approach<sup>17–19</sup> to NMR spin relaxation in proteins.<sup>20–23</sup> SRLS is the generalization of MF. Unlike MF, it allows for general tensorial properties and accounts for dynamical mode-coupling. The SRLS theory is a two-body (protein and probe) extension<sup>17–19</sup> of the standard single-body (probe only) theories for treating restricted motions.<sup>24–28</sup> Among others, one can use SRLS to determine whether given experimental data may be treated with MF. This is accomplished by applying to typical data the MF limit of SRLS and requiring physical tenability and internal consistency besides good statistics. If these conditions are not fulfilled, the symmetry of the various tensors entering the SRLS model is lowered systematically until these requirements are met. The respective parameter combination is considered appropriate in the context of the respective data sensitivity; it is used to extract properly and fully the information comprised in all of the available experimental data. Examples of this approach appear in refs 29 and 30.

We carried out in the past SRLS analyses for several proteins.<sup>20–23,29–34</sup> In all of the cases studied, we found that the tensorial properties associated with the restricted local N–H motions are not simple. In particular, the spatial restrictions exerted by the immediate protein surroundings at the site of the motion of the N–H bond are asymmetric.<sup>21–23,34</sup> This low symmetry has to be accounted for in order to describe properly <sup>15</sup>N–H backbone dynamics. We account for it by allowing for rhombic SRLS potentials. Other methods, such as molecular dynamics (MD)<sup>7,8</sup> and the 3D Gaussian axial fluctuations (GAF) model,<sup>35,36</sup> led to similar conclusions with regard to the importance of the asymmetry of the local spatial restrictions.

The asymmetry of the local ordering with compelling evidence for its importance,<sup>5–8,29–37</sup> as well as other important features, cannot be treated properly with MF. The conflicts caused by the oversimplified spectral densities prevented the analysis of combined multifield relaxation data from GB3 with standard MF.<sup>10</sup> The solution to this problem has been to allow for variations in the <sup>15</sup>N chemical shift anisotropy (CSA) tensor and to virtually eliminate the local motion.<sup>10</sup> In this study, we analyze the GB3 data of ref 10 with a standard SRLS scheme

where the magnetic tensors are constant, and provide physically well-defined information on local ordering, local motion, and local geometry.

The authors of ref 13 report in detail on local motion in GB1 based on combined <sup>15</sup>N–H relaxation data acquired in the temperature range of 278–323 K, and magnetic fields of 11.7, 14.1, and 18.8 T. However, these data are analyzed with a spectral density that has been parametrized in terms of a sum of Lorentzian functions with arbitrary decay constants and weighting factors allowed to vary in the data-fitting process. Arrhenius plots were generated from decay constants on the order of ns<sup>–1</sup>, and parameters called “activation energy” have been derived from the slopes of these plots. Here, we analyze the multifield experimental data from ref 13 with SRLS and determine activation energies for the local motion from the temperature dependence of the principal values of local diffusion tensors.

The picture of backbone dynamics in GB1 and GB3 emerging from the SRLS analysis differs qualitatively from the MF-based picture. New information associated with the local ordering, the local motion, and the local geometry is obtained. For the first time physically well-defined activation energies for local N–H motion are determined.

## 2. THEORETICAL BACKGROUND

### 2.1. The Slowly Relaxing Local Structure Approach.

The full two-body Smoluchowski SRLS theory<sup>17–19</sup> as applied to NMR spin relaxation in proteins is outlined in refs 20–23 and 37. A brief summary is given below. The SRLS frames are shown in Figure 2.

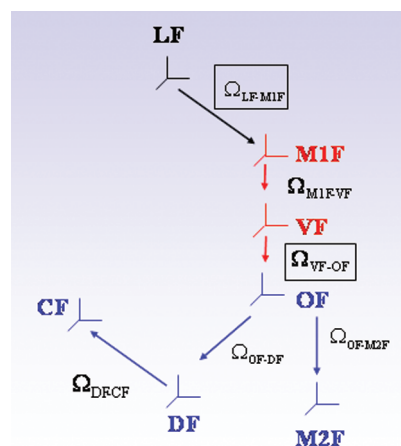


**Figure 2.** LF is the space-fixed laboratory frame with its Z-axis parallel to the external magnetic field. M1F is the principal axis system (PAS) of the global diffusion tensor,  $D_1$ . VF is the local director, given by the equilibrium orientation of the N–H bond. For isotropic global diffusion, M1F and VF are the same. The M1F and VF frames are fixed in the protein (red). The OF frame is the PAS of the local ordering tensor,  $S$ . M2F is the PAS of the local diffusion tensor,  $D_2$ . DF is the PAS of the magnetic <sup>15</sup>N–<sup>1</sup>H dipolar tensor. CF is the PAS of the <sup>15</sup>N chemical shift anisotropy tensor. OF, M2F, DF, and CF are fixed in the probe (blue). The Euler angles  $\Omega_{M1F-VF}$ ,  $\Omega_{VF-OF}$ ,  $\Omega_{OF-M2F}$ ,  $\Omega_{DF-M2F}$ , and  $\Omega_{DF-CF}$  are time-independent. The time-dependent Euler angles,  $\Omega_{LF-M1F}$ , are modulated by the global motion. The distributed Euler angles,  $\Omega_{VF-OF}$ , are associated with the local ordering.

For describing the local motion, we use a relative (probe versus protein) coordinate scheme; that is,  $\Omega_{M1F-OF}(t) = \Omega_{LF-OF}(t) - \Omega_{LF-M1F}(t)$ <sup>21–23,37</sup> (the angles  $\Omega_{LF-OF}(t)$  represent

the combined rotations represented by  $\Omega_{\text{LF-MIF}}(t)$  and  $\Omega_{\text{MIF-OF}}(t)$ . Each axial rotator when uncoupled is associated with three decay rates,  $\tau_K^{-1} = 6D_{\perp} + K^2(D_{\parallel} - D_{\perp})$ ,  $K = 0, 1, 2$ , where  $D$  stands for either the global ( $D_1$ ) or local ( $D_2$ ) diffusion tensors.<sup>21–23,37</sup> The two rotators are coupled by the potential of mean torque (POMT),  $U(\Omega_{\text{VF-OF}})$ . The diffusion equation for the coupled system is given by<sup>17–23,37</sup>

$$\frac{\partial}{\partial t}P(X, t) = -\hat{\Gamma}P(X, t) \quad (1)$$

where  $X$  is a set of coordinates completely describing the system. One has

$$\begin{aligned} X &= (\Omega_{\text{VF-OF}}, \Omega_{\text{LF-VF}}) \\ \hat{\Gamma} &= \hat{J}^t(\Omega_{\text{VF-OF}})D_2P_{\text{eq}}\hat{J}(\Omega_{\text{VF-OF}})P_{\text{eq}}^{-1} \\ &\quad + [\hat{J}(\Omega_{\text{VF-OF}}) - \hat{J}(\Omega_{\text{LF-VF}})]^t D_1 \\ &\quad \times P_{\text{eq}}[\hat{J}(\Omega_{\text{VF-OF}}) - \hat{J}(\Omega_{\text{LF-VF}})]P_{\text{eq}}^{-1} \end{aligned} \quad (2)$$

where  $\hat{J}(\Omega_{\text{VF-OF}})$  and  $\hat{J}(\Omega_{\text{LF-VF}})$  are the angular momentum operators for the probe and the protein, respectively. Note that  $\Omega_{\text{LF-VF}} = \Omega_{\text{LF-MIF}} + \Omega_{\text{MIF-VF}}$ . (That is,  $\Omega_{\text{LF-VF}}$  represents the combined effects of rotations by both sets of Euler angles on the right of this equation, where  $\Omega_{\text{MIF-VF}}$  is time-independent).

The Boltzmann distribution is  $P_{\text{eq}} = \exp[-U(\Omega_{\text{VF-OF}})/k_B T] / \langle \exp[-U(\Omega_{\text{VF-OF}})/k_B T] \rangle$ , where  $\langle \dots \rangle$  means averaging over  $\Omega_{\text{VF-OF}}$ . In general, the potential  $U(\Omega_{\text{VF-OF}})$  is expanded in the full basis set of the Wigner rotation matrix elements. When only the  $L = 2$  terms are preserved, one has<sup>21–23,37</sup>

$$\begin{aligned} u(\Omega_{\text{VF-OF}}) &= \frac{U(\Omega_{\text{VF-OF}})}{k_B T} \approx -c_0^2 D_{0,0}^2(\Omega_{\text{VF-OF}}) \\ &\quad - c_2^2 [D_{0,2}^2(\Omega_{\text{VF-OF}}) + D_{0,-2}^2(\Omega_{\text{VF-OF}})] \end{aligned} \quad (3)$$

The coefficient  $c_0^2$  evaluates the strength of the POMF, and  $c_2^2$  its nonaxiality.

The local order parameters are defined as<sup>21–23,27,28,37</sup>

$$\begin{aligned} \langle D_{0m}^2(\Omega_{\text{VF-OF}}) \rangle \\ = \int d\Omega_{\text{VF-OF}} D_{0m}^2(\Omega_{\text{VF-OF}}) \exp[-u(\Omega_{\text{VF-OF}})] \\ / \int d\Omega_{\text{VF-OF}} \exp[-u(\Omega_{\text{VF-OF}})] \end{aligned} \quad (4)$$

For at least 3-fold symmetry around the local director and at least 2-fold symmetry around the  $Z$ -axis of the local ordering frame, only  $S_0^2 \equiv \langle D_{00}^2(\Omega_{\text{VF-OF}}) \rangle$  and  $S_2^2 \equiv \langle D_{02}^2(\Omega_{\text{VF-OF}}) + D_{0-2}^2(\Omega_{\text{VF-OF}}) \rangle$  survive for  $L = 2$ .<sup>26–28</sup> The Saupe scheme order parameters relate to  $S_0^2$  and  $S_2^2$  as  $S_{xx} = (3/2)^{1/2} S_2^2 - S_0^2/2$ ,  $S_{yy} = -((3/2)^{1/2} S_2^2 + S_0^2)/2$  and  $S_{zz} = S_0^2$ .<sup>27</sup>

Equation 1 is solved to yield the SRLS time correlation functions that lead by Fourier transformation to the spectral densities,  $j_{K,K'}(\omega) = \sum_i ((c_{K,K'} \tau_i) / (1 + \omega^2 \tau_i^2))$ .<sup>21–23,37</sup> In practice, a finite number of terms is sufficient for numerical convergence of the solution. The  $j_{K,K'}(\omega)$  functions are assembled into the measurable spectral densities according to the local geometry (e.g., see Chapter 12 of ref 28). For N–H bond dynamics, the relevant measurable spectral densities are

$J^{\text{DD}}(\omega)$  for the  $^{15}\text{N}$ – $^1\text{H}$  dipolar interaction and  $J^{\text{CC}}(\omega)$  for the  $^{15}\text{N}$  CSA interaction.  $J^{\text{DD}}(\omega)$  depends on the Euler angles  $\Omega_{\text{OF-DF}}$ ;  $J^{\text{CC}}(\omega)$  depends on the Euler angles  $\Omega_{\text{OF-DF}}$  and  $\Omega_{\text{DF-CF}}$ .

Cross-correlated spin relaxation, featuring  $J^{\text{XY}}(\omega)$ , is treated in complete analogy with autocorrelated spin relaxation.<sup>21,37</sup> Thus, the calculation of  $J^{\text{DD}}(\omega)(J^{\text{CC}}(\omega))$  from the  $j_{KK'}(\omega)$  functions is based on the Wigner rotation  $R(\Omega_{\text{OF-DF}})$ . ( $R(\Omega_{\text{OF-CF}})$ ), whereas the calculation of  $J^{\text{DC}}(\omega)$  from the  $j_{KK'}(\omega)$  functions is based on the Wigner rotation  $R(\Omega_{\text{OF-DF}})$  followed by the Wigner rotation  $R(\Omega_{\text{DF-CF}})$ .

For rhombic local ordering and axial (e.g., dipolar) magnetic interaction six distinct pairs,  $K, K' = (0,0), (1,1), (2,2), (0,2), (-1,1)$ , and  $(-2,2)$ , have to be considered. In this case, the explicit expression for  $J^{\text{DD}}(\omega)$  is

$$\begin{aligned} J^{\text{DD}}(\omega) &= (d_{00}^2(\beta_{\text{OF-DF}}))^2 j_{00}(\omega) \\ &\quad + 2(d_{10}^2(\beta_{\text{OF-DF}}))^2 j_{11}(\omega) \\ &\quad + 2(d_{20}^2(\beta_{\text{OF-DF}}))^2 j_{22}(\omega) \\ &\quad + 4d_{00}^2(\beta_{\text{OF-DF}})d_{20}^2(\beta_{\text{OF-DF}})j_{02}(\omega) \\ &\quad + 2d_{-10}^2(\beta_{\text{OF-DF}})d_{10}^2(\beta_{\text{OF-DF}})j_{-11}(\omega) \\ &\quad + 2d_{-20}^2(\beta_{\text{OF-DF}})d_{20}^2(\beta_{\text{OF-DF}})j_{-22}(\omega) \end{aligned} \quad (5)$$

The autocorrelated  $^{15}\text{N}$ – $^1\text{H}$  relaxation parameters  $T_1$ ,  $T_2$ , and  $^{15}\text{N}$ – $\{^1\text{H}\}$  NOE are calculated as a function of  $J^{\text{DD}}(0)$ ,  $J^{\text{DD}}(\omega_{\text{H}})$ ,  $J^{\text{DD}}(\omega_{\text{N}})$ ,  $J^{\text{DD}}(\omega_{\text{H}} - \omega_{\text{N}})$ ,  $J^{\text{DD}}(\omega_{\text{H}} + \omega_{\text{N}})$ ,  $J^{\text{CC}}(0)$ ,  $J^{\text{CC}}(\omega_{\text{N}})$  and the magnetic interactions, using standard expressions for NMR spin relaxation.<sup>38–40</sup> The cross-correlated relaxation rates associated with N–H bond dynamics,  $\eta_{xy}$ <sup>41</sup> and  $\eta_{\omega}$ <sup>42</sup> feature the measurable spectral density obtained as outlined above, and the  $^{15}\text{N}$ – $^1\text{H}$  dipolar/ $^{15}\text{N}$  CSA magnetic interaction cross-term.

Our most recent fitting scheme for SRLS,<sup>37</sup> used in the present study, comprises important enhancements including the separation of the local ordering and the local diffusion frames, the addition of  $L = 4$  terms to the expression for the local potential, and independent hydrodynamics-based calculations of the global diffusion tensor. We call this software package C++OPPS (COupled Protein Probe Smoluchowski). It is available at the Web site <http://www.chemica/unipd.it/licc/software.html> and described in detail in ref 37.

**2.2. Model-Free.** The MF approach gives directly the measurable spectral density  $J(\omega) = J^{\text{DD}}(\omega) = J^{\text{CC}}(\omega)$ , made up of two Lorentzian terms that represent the global motion, and a single effective local motion.<sup>14,15</sup> This simple form is based on the premise that these dynamic processes are statistically independent, by virtue of being time scale separated.<sup>14</sup> All of the tensorial properties are simple. Thus, the global diffusion is isotropic, the local motion is isotropic, the local ordering is axial, and its principal axis points along the principal axis of all the collinear axial magnetic tensors involved. In this limit, the MF spectral density is given by<sup>14</sup>

$$J(\omega) = S^2 \tau_m / (1 + \tau_m^2 \omega^2) + (1 - S^2) \tau_e / (1 + \tau_e^2 \omega^2) \quad (6)$$

The parameter  $\tau_m$  is the correlation time for the global motion, and  $\tau_e \ll \tau_m$  is the effective correlation time for the local motion. By virtue of  $\tau_e \ll \tau_m$ , one has  $1/\tau_e = 1/\tau_m + 1/\tau_e \sim 1/\tau_e$ .  $S^2$  is defined as the plateau value,  $C^L(\infty)$ , to which the local motional



time correlation function,  $C^L(t)$ , converges at long times. Mathematically  $C^L(\infty)$  is given by  $\sum_{m=0,\pm 1,\pm 2} |\langle Y_{2m}(\theta, \varphi) \rangle \langle Y_{2m}^*(\theta, \varphi) \rangle|$  where  $Y_{2m}$  are the spherical harmonics of Brink and Satchler.<sup>43</sup> The “generalized” order parameter is defined as  $S \equiv (C^L(\infty))^{1/2}$ .<sup>14</sup>  $S^2$  is considered to represent the amplitude of the local motion. In the context of the physical meaning of  $S$ ,<sup>44</sup> this interpretation is appropriate when the POMT is axial and strong, and the local motion is so fast that its effect on the spin relaxation is completely averaged out.<sup>19</sup> On the basis of the theory of moments,  $\tau_e$  is defined as the area of the exact time correlation function for internal motion (corresponding to a “frozen” protein<sup>14</sup>) divided by  $(1 - S^2)$ .

The extended model-free (EMF) spectral density is given by<sup>16</sup>

$$J(\omega) = S_f^2 [S_s^2 \tau_m / (1 + \omega^2 \tau_m^2) + (1 - S_s^2) \tau_s^1 / (1 + \omega^2 \tau_s^2)] + (1 - S_f^2) \tau_f^1 / (1 + \omega^2 \tau_f^2) \quad (7)$$

The parameter  $\tau_f$  ( $\tau_f^1$ ) is the (effective) correlation time for fast local motion. The parameter  $\tau_s$  ( $\tau_s^1$ ) is the (effective) correlation time for slow local motion.  $S_s^2$  and  $S_f^2$  are squared generalized order parameters associated with these motions. One has  $1/\tau_f^1 = 1/\tau_f + 1/\tau_m \sim 1/\tau_f$  and  $1/\tau_s^1 = 1/\tau_s + 1/\tau_m$ . The large time scale separation assumption requires that  $\tau_f^1 \ll \tau_m$  and  $\tau_s^1 \ll \tau_m$ . Yet, the EMF formula is used typically when  $\tau_s^1$  and  $\tau_m$  occur on the same time scale. In addition, the third term of eq 7 is often omitted under the assumption that  $\tau_f^1$  is very small, obtaining thereby the reduced EMF formula.

### 3. RESULTS AND DISCUSSION

**3.1. Global Diffusion.**  $^{15}\text{N}$   $T_1$ ,  $T_2$ ,  $^{15}\text{N}-\{^1\text{H}\}$  NOE,  $\eta_{xy}$  and  $\eta_z$  from GB3 were acquired in ref 9 at 14.1 T and 297 K. The experimental  $R_2 = 1/T_2$  values of the  $^{15}\text{N}$ -H sites in the  $\alpha$ -helix were found to be substantially larger than the average  $R_2$  value for the other parts of polypeptide chain (cf. Figure 3b). This

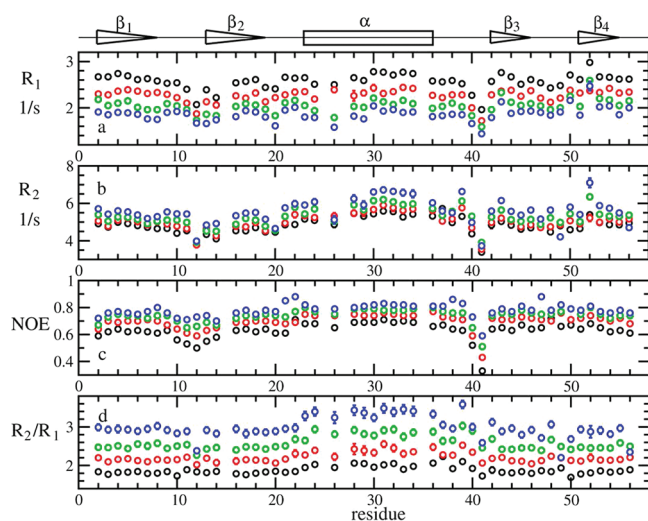


**Figure 3.** Experimental  $^{15}\text{N}$   $R_1$  (a),  $R_2$  (b),  $^{15}\text{N}-\{^1\text{H}\}$  NOE (c), and  $R_2/R_1$  (d) data taken from the Supporting Material of ref 10: 11.7 T - black, 14.1 T - red, 16.4 T - green, and 18.8 T - blue.

was ascribed<sup>9</sup> to either conformational exchange contributions ( $R_{ex}$ ) to  $R_2$ , or deviation of the global diffusion tensor,  $D_1$ , from spherical symmetry (given that the N-H bonds within the  $\alpha$ -helix are tilted from the Z-axis of the axial  $D_1$  tensor by only

23°, their  $R_2$  values will be larger than the average value if  $D_1$  is axially symmetric).

The latter option was adopted, considering the  $R_{ex}$  contributions obtained when  $D_1$  was taken isotropic to be artificial.<sup>9</sup> The calculated values of  $R_1 = 1/T_1$  and  $R_2$  were replaced with  $R_1'$  and  $R_2'$ , obtained by omitting the high-frequency terms from the spectral density.  $R_1'$  and  $R_2'$  were used to determine  $\tau_m = 1/(6D_1(\text{app})) = 3.33 \pm 0.11$  ns,  $D_{1,\parallel}/D_{1,\perp} = 1.37 \pm 0.06$ ,  $\Theta = (69 \pm 12)^\circ$ , and  $\Phi = (94 \pm 7)^\circ$  at 297 K<sup>9</sup> (where the angles  $\Theta$  and  $\Phi$  determine the orientation of the (axial) global diffusion frame (M1F in Figure 2) in the inertia tensor frame of the crystal structure with PDB code 1IGD<sup>1</sup>).

The following comments are in order.

1. The authors of ref 9 note that the experimental  $R_1$  profile does not comply with expectations implied by an axial  $D_1$  tensor. This feature has been interpreted using arguments based on the oversimplified MF spectral density. They also indicate that standard MF treatment was applied to the loop residues of GB3 using either isotropic or axial global diffusion. The corresponding squared order parameters were found to differ slightly, and the overall conclusions did not change significantly. In general, the  $S^2$  profiles obtained using isotropic or axial  $D_1$  are very similar, except for somewhat larger  $S^2$  values for the  $\alpha$ -helix in the axial  $D_1$  case. One may conclude that the overall picture of backbone dynamics in GB3 is affected to a small extent by using axial  $D_1$  with  $D_{1,\parallel}/D_{1,\perp} = 1.37$  instead of isotropic  $D_1$ .
2. The average  $R_2$  experimental value,  $\langle R_2(\text{exp}) \rangle$ , equals  $5.5 \text{ s}^{-1}$ .<sup>9</sup> The average  $R_{ex}$  value is  $0.4 \text{ s}^{-1}$ ; this represents only 7.2% of  $\langle R_2(\text{exp}) \rangle$  (the reported error in  $D_1(\text{app})$  is 3.3% and the reported error in  $D_{1,\parallel}/D_{1,\perp}$  is 4.4%). The inaccuracies implied by the oversimplified MF spectral density exceed by far 7.2%.<sup>21,22</sup> Note also that  $R_{ex}$  was obtained using  $R_1'$  and  $R_2'$ , that is, simplifying further the already oversimplified MF formula.<sup>9</sup> Hence, the  $R_{ex}$  contributions are small and their presence does not justify taking  $D_1$  axial instead of isotropic.
3.  $R_{ex}$  terms obtained with MF analysis were shown previously to absorb the unaccounted for asymmetry of the local ordering. This was demonstrated quantitatively for *Escherichia coli* ribonuclease H and the CORE domain of *E. coli* adenylate kinase (AKeco). Methods for distinguishing among the effects of a nonspherical  $D_1$  tensor, a rhombic local ordering tensor, and  $R_{ex}$  contributions, have been devised.<sup>45</sup> The possibility that the  $R_{ex}$  terms might have absorbed factors other than  $D_1$  axially is not considered in ref 9.
4. Seewald et al.<sup>12</sup> studied  $^{15}\text{N}$  spin relaxation from GB1. Experimental data were acquired at 273, 283, 293, 303, 313, and 323 K, and 14.1 T. The  $R_2/R_1$  profiles obtained at 273 and 283 K resemble the corresponding  $R_2$  and  $\eta_{xy}$  profiles because  $R_1$  of GB1 is near its (approximate) minimum at the respective experimental conditions, hence virtually constant. Above 283 K, the  $R_2/R_1$  profile is within a good approximation constant (Figure 2 of ref 12). This is a strong indication that one may consider the global diffusion tensor of GB1 to be isotropic. A similar scenario is likely to occur for GB3, with the temperature at which  $R_1$  is no longer near its (approximate) minimum being somewhat higher.

Using the traditional  $^{15}\text{N}$   $R_2/R_1$ -based MF method, Seewald et al.<sup>12</sup> determined  $\tau_m = 4.19$  (3.21) ns at 293 (303) K and  $D_{\parallel}/D_{\perp} = 1.27$  for all the temperatures studied.

5. Barchi et al.<sup>11</sup> studied  $^{15}\text{N}$  spin relaxation from GB1 using combined data acquired at magnetic fields of 11.7 and 14.1 T, and 299 K. These authors used isotropic global diffusion with  $\tau_m = 3.3$  ns. The data-fitting process yielded  $R_{\text{ex}}$  contributions mostly below  $0.15 \text{ s}^{-1}$ ; this value is on the order of the reported error in  $^{15}\text{N}$   $R_2$ .  $R_{\text{ex}}$  contributions of approximately  $0.37 \text{ s}^{-1}$  were determined for residues A24, A26, and V29 of the  $\alpha$ -helix. The  $R_{\text{ex}}$  values of residues A24 and A26 are likely to overcome unduly small  $S^2$  values located at the minima of an alternating pattern unexpected for a regular  $\alpha$ -helix. Hence, these small  $S^2$  values, and consequently the corresponding  $R_{\text{ex}}$  terms, are likely to result from experimental data that have been force-fitted. Residue V29 has maximum  $^{15}\text{N}$ - $\{^1\text{H}\}$  NOE at 14.1 T. We have shown previously that MF does not evaluate properly the maximum  $^{15}\text{N}$ - $\{^1\text{H}\}$  NOE.<sup>21</sup> The constraints imposed on the fitting process by the inappropriate upper NOE limit might have yielded an artificial  $R_{\text{ex}}$  term. Thus, the results of the  $^{15}\text{N}$  relaxation analysis carried out in ref 11 are consistent with isotropic  $D_{\parallel}$ .

On the basis of the evidence and considerations outlined above, we use  $D_{\parallel} = (5.01 \pm 0.03) \times 10^7 \text{ s}^{-1}$  (which corresponds to  $\tau_m = 3.33$  ns) as the global diffusion rate in our calculations.

**3.2. Restricted Local Motion.** Diffusive local motion is considered. This is the most general type of motional model. One can devise simpler models (“wobble-in-a-cone”, motion on the surface of a cone, jumps among symmetry-related sites, etc.) by devising appropriate potentials forms. For example, see Figure 4 of ref 18 and associated discussion.

As pointed out above, we require good statistics, physical tenability, and internal consistency. In addition, we require that the various GB3 data set comprising data acquired at 16.4 and 18.8 T; 14.1, 16.4, and 18.8 T; and 11.7, 14.1, 16.4, and 18.8 T (taken from ref 10) yield best-fit parameters within the estimated error limits (see below). We found that including the 9.4 T data often increases substantially the uncertainty in the best-fit parameters; these data were disregarded (similar problems were encountered in the MF analysis; for example, see Figure 9b of ref 10). The results presented below were obtained in most cases with the combined four-field data set illustrated in Figure 3. In some cases, we used the three-field data set. The experimental data were analyzed with good statistics (typically  $\chi^2/\text{df}$ , where df denotes the number of degrees of freedom, below the 0.05 critical value) using the constant established  $^{15}\text{N}$  CSA tensor value of  $-172.0$  ppm, the N–H bond length of  $1.02 \text{ \AA}$  (ref 46), and the angle  $\beta_{\text{CSA}} \equiv \beta_{\text{DF-CF}} = -17.0^\circ$  (ref 21).

Table 1 illustrates the independence of the results on the experimental data set used, with residues T16 and A29 serving as an example. For these residues, the results are virtually the same for combined two-, three-, and four-field data. In other cases, there are small differences among results obtained using different data sets. However, all of the best-fit parameters reported in this study are within the estimated error limits determined as the uncertainty associated with variations in the respective starting values. These values are  $5.0 \times 10^8 \text{ s}^{-1} \leq D_2 \leq 1.0 \times 10^{11} \text{ s}^{-1}$ ,  $\beta_D = -101.3^\circ$ , and  $c_0^2$  and  $c_2^2$  taken as those values that yielded the lowest  $\chi^2/\text{df}$  value in a preliminary manual search procedure. On the basis of the results obtained

**Table 1. Results of SRLS-Based Data-Fitting Using the  $^{15}\text{N}$ –H Relaxation Data of Residues T16 (Strand  $\beta_2$ ) and A29 ( $\alpha$ -Helix), Acquired at the Magnetic Fields<sup>10</sup> Depicted in the First Column<sup>a</sup>**

magnetic fields for data acquisition	$D_2 \times 10^{-8} \text{ s}^{-1}$	$S_0^2$	$\beta_D$ , deg	$\chi_{\text{red}}^2$
<b>T16</b>				
16.4 and 18.8 T	10.56	0.895	−2.5	2.627
14.1, 16.4, and 18.8 T	10.80	0.895	−2.1	1.711
11.7, 14.1, 16.4, and 18.8 T	10.33	0.893	−2.9	2.166
<b>A29</b>				
16.4 and 18.8 T	5.47	0.931	8.8	0.944
14.1, 16.4, and 18.8 T	5.56	0.929	8.3	1.633
11.7, 14.1, 16.4, and 18.8 T	5.61	0.928	7.9	1.585

<sup>a</sup>Shown are the best-fit local motional rate ( $D_2$ ); the axial order parameter ( $S_0^2$ ); the angle between the main ordering axis and the principal axis of the dipolar  $^{15}\text{N}$ – $^1\text{H}$  tensor ( $\beta_D$ ); and  $\chi^2/\text{df}$ .  $c_0^2$ ,  $D_2$ , and  $\beta_D$  were allowed to vary; we call this scheme “diffusion tilt”.

for 6–12 starting value sets, we estimate the errors in  $D_2$ ,  $c_0^2$ ,  $c_2^2$ , and  $\beta_D$  ( $\Delta\beta_D$ ) to be 11, 15, 5, and 3%, respectively. The errors in  $S_0^2$  and  $S_2^2$  are estimated to be 1%. They are significantly smaller than the errors in  $c_0^2$  and  $c_2^2$ , as implied by the functional dependence of the order parameters on the potential coefficients in the limit of strong ordering and large rhombicity.<sup>21</sup>

We proceed presenting the results of the SRLS-based data-fitting calculations. As indicated above, the global diffusion rate was taken from ref 9 as  $D_{\parallel} = (5.01 \pm 0.03) \times 10^7 \text{ s}^{-1}$ . The first parameter combination employed includes  $c_0^2$  (which describes axial local ordering with the main ordering axis along the N–H bond) and  $D_2$  (which describes isotropic local diffusion) as variables. We call it “model 2”, as this is the formal analogue of model 2 in MF, where  $S^2$  and  $\tau_c$  are allowed to vary.<sup>47,48</sup> The SRLS potential is given by the first term of eq 3, and the axial order parameter,  $S_0^2$ , is given by eq 4 with  $m = 0$ .

Typical results are shown in rows 1 and 2 of Table 2 for the N–H bonds of residue L5 of the strand  $\beta_1$ , and residue A29

**Table 2. Results of SRLS-Based Data-Fitting for the Residues and Parameter Combinations Depicted in the Second Column<sup>a</sup>**

no.	parameter combination and residue designation	$D_2 \times 10^{-8} \text{ s}^{-1}$ ; $r$	$S_0^2$	$S_2^2$	$\beta_D$ , deg	$\chi_{\text{red}}^2$
1	model 2, L5, $\beta_1$	9.36; 0.053	0.915	0		0.898
2	model 2, A29, $\alpha$ -helix	8.78; 0.057	0.927	0		2.154
3	diff. tilt, T16, $\beta_2$	10.80; 0.046	0.895	0	−2.1	1.711
4	diff. tilt, T44, $\beta_3$	11.11; 0.045	0.911	0	−0.7	2.341
5	diff. tilt, A29, $\alpha$ -helix	5.56; 0.090	0.929	0	8.3	1.633
6	diff. tilt, K31, $\alpha$ -helix	3.87; 0.129	0.955	0	6.5	0.488
7	diff. tilt, V39, $\alpha$ -helix/ $\beta_3$	3.33; 0.150	0.921	0	6.5	1.836
8	diff. tilt, D40, $\alpha$ -helix/ $\beta_3$	10.53; 0.048	0.851	0	0.7	13.506
9	diff. tilt, G41, $\alpha$ -helix/ $\beta_3$	3.64; 0.138	0.807	0	−13.6	16.270
10	rh. potential, L5, $\beta_1$	11.00; 0.046	−0.484	1.106	−90.5	0.809
11	rh. potential, T16, $\beta_2$	13.37; 0.037	−0.485	1.066	−96.6	0.444
12	rh. potential, T44, $\beta_3$	15.06; 0.033	−0.484	1.107	−91.1	0.668
13	rh. potential, A29, $\alpha$ -helix	5.49; 0.091	−0.449	1.151	−97.8	0.931
14	rh. potential, K31, $\alpha$ -helix	4.04; 0.124	−0.475	1.171	−96.5	0.505

<sup>a</sup>Shown are the best-fit local motional rate,  $D_2$ , and the time scale separation,  $r = D_1/D_2$ ; the axial order parameter,  $S_0^2$ ; the rhombic order parameter,  $S_2^2$ ; the angle between the main local ordering axis and the principal axis of the  $^{15}\text{N}$ – $^1\text{H}$  dipolar frame,  $\beta_D$ ; and  $\chi^2/\text{df}$ .

of the  $\alpha$ -helix, respectively. The ratio,  $r$ , between the global ( $D_1$ ) and the local ( $D_2$ ) motional rates (i.e., the time scale separation) is 0.053 for L5 and 0.057 for A29. The best-fit parameters shown do not distinguish between the  $\alpha$ -helix and the remaining part of the polypeptide chain, as expected based on the experimental data (Figure 3b). Different data sets yield significantly different results. Importantly, the local ordering at  $^{15}\text{N}$ -H sites in proteins has been shown to be anisotropic.<sup>2,6–8</sup>

Yet, “model 2” does not represent in any way the asymmetry of the local spatial restrictions at the  $^{15}\text{N}$ -H sites. These features are unacceptable. Therefore, we do not consider “model 2” as an adequate method of analysis, although the statistical requirements are fulfilled.

Next, we also allow  $\beta_D \equiv \beta_{\text{OF-DF}}$ , which is the angle between the Z-axes of the local ordering (OF) and magnetic dipolar (DF) frames, to vary in the data-fitting process. This is the “diffusion tilt” scheme, which has the same number of variables as the MF model 5.<sup>47,48</sup> Formal analogy cannot be established because the model 5 formula is obtained from the EMF spectral density (eq 7) by omitting the third term. This does not yield a physical spectral density.<sup>21,22</sup>

Typical results obtained with the “diffusion tilt” scheme are shown in rows 3–9 of Table 2 for the N–H bonds of residues T16 of the strand  $\beta_2$  and T44 of the strand  $\beta_3$ ; residues A29 and K31 of the  $\alpha$ -helix; and residues V39, D40, and G41 of the loop  $\alpha$ -helix/ $\beta_3$ . Additional residues were analyzed in this context (not shown). In general, the best-fit parameters  $D_2$ ,  $S_0^2$ , and  $\beta_D$  do not distinguish clearly between the  $\alpha$ -helix and the remaining part of the polypeptide chain. There are quite a few inconsistencies. For example, the N–H bonds of residues D40 and G41 have quite similar experimental data but very different best-fit parameters. The angle  $\beta_D$  is expected to be close to  $-101.3^\circ$ ,<sup>21,22,34–37,49</sup> which is the standard angle between the N–H bond and the  $\text{C}_{i-1}^\alpha - \text{C}_i^\alpha$  axis. Clearly, this is not the case. We conclude that allowing for a “diffusion tilt” does not account adequately for the asymmetry of the local spatial restrictions at the  $^{15}\text{N}$ -H sites. Because of these unsatisfactory features, we do not consider the “diffusion tilt” scheme as an adequate method of analysis either, although the statistical requirements are fulfilled.

We proceed allowing the local potential to be rhombic. Its form is given by eq 3, which comprises an axial term with coefficient  $c_0^2$  and a rhombic term with coefficient  $c_2^2$ . The order parameters  $S_0^2$  and  $S_2^2$  are defined in terms of the potential coefficients  $c_0^2$  and  $c_2^2$  ( $S_0^2$  is given by eq 4 with  $m = 0$  and  $S_2^2$  is given by eq 4 with  $m = 2$ ). The parameters  $c_0^2$ ,  $c_2^2$ ,  $D_2$ , and  $\beta_D$  are allowed to vary. We call this scheme (which has the same number of variables as MF model 6 of ref 48) “rhombic potential”. The results shown in Table 2 are appropriate from a statistical point of view. The angle  $\beta_D$  differs from  $-101.3^\circ$  by less than  $11^\circ$ . There is clear distinction between the  $\alpha$ -helix residues, on the one hand, and the  $\beta$ -strand and loop residues, on the other hand. Different data sets yield similar results (not shown).

We consider the “rhombic potential” scheme as an adequate method of analysis that matches the sensitivity of the experimental data and apply it to the  $^{15}\text{N}$ -H relaxation parameters shown in Figure 3. The best-fit results are shown in Figures 4–7.

**3.2.1. Local Diffusion.** The rate of local diffusion,  $D_2$ , is shown in Figure 4a and the local motional correlation time,  $\tau = 1/(6 \times D_2)$ , is shown in Figure 4b. We depict both parameters because fast motions are better resolved when they are given by

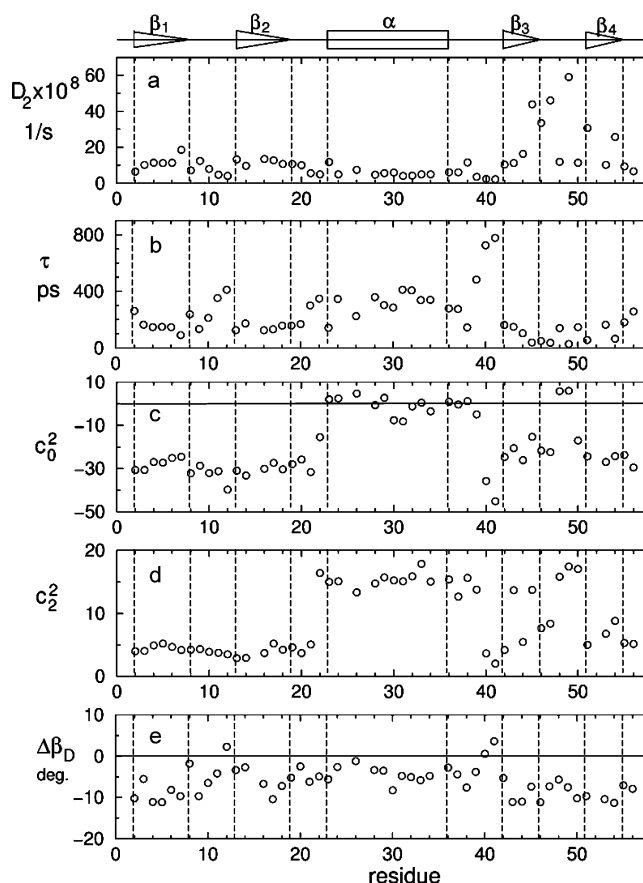


**Figure 4.** Best-fit (a) local motional rate,  $D_2$ ; (b) local motional correlation time,  $\tau$ ; (c) axial potential coefficient,  $c_0^2$ ; (d) rhombic potential coefficient,  $c_2^2$ ; (e) deviation of the main ordering axis,  $Z_{\text{OF}}$ , from the  $\text{C}_{i-1}^\alpha - \text{C}_i^\alpha$  axis,  $\Delta\beta_D$ . These results were obtained by fitting the combined data acquired at 11.7, 14.1, 16.4, and 18.8 T, and 297 K,<sup>10</sup> with the “rhombic potential” SRLS scheme. The errors in  $D_2$ ,  $\tau$ ,  $c_0^2$ ,  $c_2^2$ , and  $\Delta\beta_D$  are 10, 10, 15, 5, and 5%, respectively.

$D_2$ , whereas slow motions are better resolved when they are given by  $\tau$ . The local motional correlation time,  $\tau$ , is  $312 \pm 79$  ps for the  $\alpha$ -helix. Most of the N–H bonds belonging to  $\beta$ -strands have  $\tau$  values of  $126 \pm 44$  ps (Figure 4b). Within the strand  $\beta_2$ ,  $\tau$  is nearly constant. The same holds true for the strand  $\beta_1$ , except for its N- and C-termini, which have somewhat larger and identical  $\tau$  values. The loops have larger  $\tau$  values in the middle and smaller  $\tau$  values at their ends. Several loop residues have very large  $\tau$  values. Thus, we find that residues T11 and L12 of the loop  $\beta_1/\beta_2$  have  $\tau = 383 \pm 30$  ps; residues V21 and D22 of the loop  $\beta_2/\alpha$ -helix have  $\tau = 324 \pm 24$  ps; within the loop  $\alpha$ -helix/ $\beta_3$ , residue V39 has  $\tau = 484 \pm 49$  ps and residues D40 and G41 have  $\tau = 753 \pm 26$  ps (Figure 4b).

Two out of four residues of the loop  $\beta_3/\beta_4$  exhibit exceptionally fast local motions with correlation time of  $(32 \pm 4)$  ps (Figure 4a). As shown below, this loop also exhibits unique features of local ordering.

**3.2.2. Local Geometry.** The sixth column of rows 10–14 of Table 2, where the “rhombic potential” fitting scheme was applied, shows the best-fit values of the angle  $\beta_D$  between the principal axes of the local ordering and dipolar tensors. These values indicate that the actual main ordering axis is tilted at  $90^\circ$ – $98^\circ$  from the N–H bond. A plausible and actually expected<sup>21,22,34–37,49</sup> assignment is the  $\text{C}_{i-1}^\alpha - \text{C}_i^\alpha$  axis, with a standard tilt of  $101.3^\circ$  from the N–H bond. The angle  $\beta_D$  varies



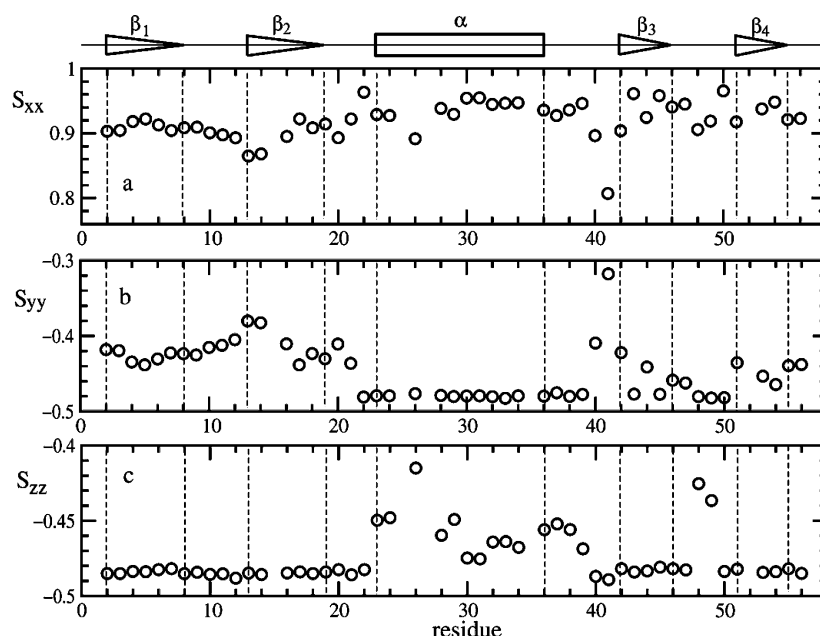


**Figure 5.** Principal values of the Saupe scheme ordering tensor (a)  $S_{xx}$  (b)  $S_{yy}$  and (c)  $S_{zz}$  calculated from the  $c_0^2$  and  $c_2^2$  values shown in Figure 4c,d, as outlined in the text. The errors are 1%.

throughout the polypeptide chain between  $-91^\circ$  and  $-101^\circ$ ; only residues L12 and G41 have  $\beta_D$  values more negative than  $-101.3^\circ$ . Instead of  $\beta_D$  we show in Figure 4e the deviation,  $\Delta\beta_D$ , of the actual main ordering axis from the  $C_{i-1}^\alpha - C_i^\alpha$  axis. For the  $\alpha$ -helix,  $\Delta\beta_D$  equals  $(-4 \pm 2)^\circ$ . For the  $\beta$ -strands  $\Delta\beta_D$  is twice as large,  $(-8 \pm 3)^\circ$ .

The angle  $\Delta\beta_D$  is the only parameter that is not uniform within the strands  $\beta_1$  and  $\beta_2$ . It varies considerably within all of the  $\beta$ -strands (Figure 4). As discussed below, we find evidence for hydrogen-bonds (H-bonds) stabilizing the  $\beta$ -sheet structurally. The variations in  $\Delta\beta_D$  might partly counterbalance these constraints. For the  $\alpha$ -helix,  $\Delta\beta_D$  is relatively small. In this case, the out-of-peptide-bond-plane excursions of the instantaneous N–H bond orientation<sup>2</sup> are likely to counter-balance packing constraints.

It should be pointed out that  $\beta_D$  defines an effective orientation implied by the complexity of the local motion, rather than a physical axis that is part of the protein structure.

**3.2.3. Local Ordering.** The asymmetry of the local spatial restrictions is substantiated in SRLS in terms of rhombic ordering. As shown above, the main local ordering axis is nearly parallel to the  $C_{i-1}^\alpha - C_i^\alpha$  axis. This assignment is supported by numerous previous SRLS studies where  $\beta_D$  was allowed to vary,<sup>21,22,31–34,37</sup> and by the 3D GAF model, where this geometric feature is encoded.<sup>35,36</sup> The components of the Saupe scheme local ordering tensor are shown in Figure 5. The fact that  $S_{xx}$  is large and positive indicates that  $X_{OF}$  is the main ordering axis of the  $S$  tensor for all of the N–H bonds of GB3. Thus,  $X_{OF}$  points along  $C_{i-1}^\alpha - C_i^\alpha$ .  $Z_{OF}$  is defined in the SRLS frame scheme to point along the N–H bond. Both  $X_{OF}$  and  $Z_{OF}$  lie within the peptide-bond plane. Hence,  $Y_{OF}$  is perpendicular to that plane.

Within the  $\alpha$ -helix one has  $\langle S_{xx} \rangle = 0.941$  with relatively small variations in  $S_{xx}$ ,  $\langle S_{yy} \rangle = -0.480$  with virtually no variation in  $S_{yy}$ , and  $\langle S_{zz} \rangle = -0.461$  with variations in  $S_{zz}$  that are relatively large compared with the rest of the polypeptide chain (Figure 5). Clearly, strong ordering prevails at the  $^{15}\text{N}$ –H sites of the  $\alpha$ -helix around both  $X_{OF}$  and  $Y_{OF}$ . Except for residues

A48 and T49 of the loop  $\beta_3/\beta_4$  and the N-terminal part of the loop  $\alpha$ -helix/ $\beta_3$ , the N–H bonds outside of the  $\alpha$ -helix have quite different values of  $S_{yy}$  and  $S_{zz}$  as compared to the N–H bonds within the  $\alpha$ -helix (Figure 5b,c). While  $S_{yy}$  is relatively uniform within the strand  $\beta_1$ , it varies significantly in the remaining part of the  $\beta$ -sheet.  $S_{zz}$  is virtually uniform and equal to  $-0.485 \pm 0.002$  in the  $\beta$ -sheet (except for residues A48 and T49).

Within the strand  $\beta_1$  and the loop  $\beta_1/\beta_2$  the ordering is relatively large, with  $0.90 \leq S_{xx} \leq 0.92$ , and quite rhombic with  $-0.44 \leq S_{yy} \leq -0.40$  and  $S_{zz} = -0.485 \pm 0.005$  (Figure 5). In all of the other  $\beta$ -strands, and in the loops that connect the various secondary structure elements,  $S_{xx}$  varies between 0.860 and 0.960. The  $S_{zz}$  values of residues A48 and T49 of the loop  $\beta_3/\beta_4$  are  $-0.425$  and  $-0.437$ , respectively; these values are exceptionally small. The local potential strength and rhombicity (Figure 4c,d) and the local ordering (Figure 5) of residues A48 and T49 of the loop  $\beta_3/\beta_4$  are similar to the corresponding properties of the  $\alpha$ -helix rather than the corresponding properties of the other loops of GB3. The biological function of the loop  $\beta_3/\beta_4$  might require structural and kinetic properties similar to those of the  $\alpha$ -helix.

The diagonal local ordering tensor components determined using SRLS distinguish among the various secondary structure elements. The ordering around  $C_{i-1}^\alpha - C_i^\alpha$  ( $S_{xx}$ ) is on average larger for the  $\alpha$ -helix and the strands  $\beta_3$  and  $\beta_4$ , and smaller for the strands  $\beta_1$  and  $\beta_2$  (Figure 5a). The ordering around the N–H bond orientation ( $S_{zz}$ ) is large and constant within the  $\beta$ -sheet, except for residues A48 and T49. It is smaller and exhibits relatively large variations for the  $\alpha$ -helix (Figure 5c). The opposite pattern is observed for the ordering around the orientation perpendicular to the peptide-bond plane ( $S_{yy}$ ) (Figure 5b).

The strand  $\beta_1(\beta_3)$  is connected to the strand  $\beta_2(\beta_4)$  at its N-terminus. The strand  $\beta_1(\beta_4)$  is connected to the strands  $\beta_2$  and  $\beta_4$  ( $\beta_1$  and  $\beta_3$ ) at its N-, and C-terminus, respectively. Let us compare that pair  $\beta_1$  and  $\beta_4$  with the pair  $\beta_2$  and  $\beta_3$ . Inspection of the ribbon diagram of the GB3 backbone (Figure 1)

shows that the C-terminal part of the strand  $\beta_2$  packs against the N-terminal part of the  $\alpha$ -helix and connects to the strand  $\beta_1$  through a rather stretched four-residue-long loop. The ensuing interactions are likely to impart rigidity to the backbone segment comprising the strand  $\beta_1$  and the loop  $\beta_1/\beta_2$ , in agreement with all of the Saupe scheme order parameters being nearly constant for this chain segment (Figure 5).

$S_{xx}$  varies to a relatively large extent within the chain segment comprising the strands  $\beta_3$  and  $\beta_4$ , and the intervening loop  $\beta_3/\beta_4$ . The N- and C-terminal N–H bonds of the strands  $\beta_1$  and  $\beta_4$  have virtually the same  $S_{xx}$ ,  $S_{yy}$ , and  $S_{zz}$  values. No such feature is observed for the strands  $\beta_2$  and  $\beta_3$ . The correlation of rigidity with similarly constrained ends of  $\beta$ -strands is an interesting structural property not revealed so far.

The strand  $\beta_2$  has been implicated in the binding of GB3 to its cognate Fab fragment.<sup>2</sup> This might be related to the relatively large variations in  $S_{xx}$  and  $S_{yy}$  (Figure 5a,b), which eventually facilitate the structuring of the binding site. An RDC-based investigation found that the strand  $\beta_2$  experiences asymmetric motion perpendicular to the chain orientation.<sup>2</sup> This might be related to different patterns exhibited by  $S_{yy}$  and  $S_{zz}$  which represent the ordering within the plane perpendicular to the chain orientation.

The fact that  $S_{zz}$  associated with the N–H bond direction, is close to the maximum value of  $-0.5$  for the  $\beta$ -sheet supports the dominant role played by H-bonds in stabilizing  $\beta$ -sheets in proteins. The order parameters of the  $\alpha$ -helix also have interesting structural implications. The regions flanking the  $\alpha$ -helix (including the residues D22, N37, G38, and V39) have order parameters largely similar to those of the  $\alpha$ -helix (Figures 5 and 6).  $S_{xx}$  and  $S_{yy}$  are nearly as large as allowed

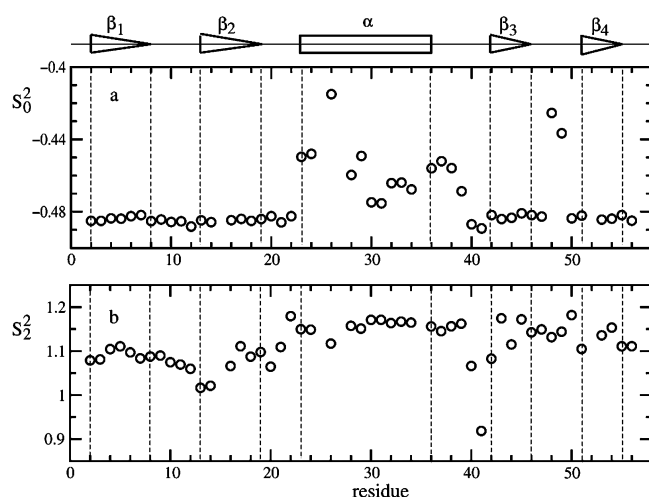


**Figure 6.** Principal values of the Wigner scheme ordering tensor components  $S_0^2$  (a) and  $S_2^2$  (b), calculated from the  $c_0^2$  and  $c_2^2$  values shown in Figure 4c,d, as outlined in the text. The errors are 1%.

theoretically (1 and  $-0.5$ , respectively), providing evidence for a well-structured  $\alpha$ -helix. In contrast, the order parameter  $S_{zz}$ , which evaluates the strength of the local ordering around the N–H bond, is relatively weak and varies substantially (Figure 5c). This is consistent with out-of-peptide-bond-plane N–H bond excursions of  $10$ – $15^\circ$  detected with RDC studies.<sup>2</sup> That the N-terminal part of the  $\alpha$ -helix has on average relatively small  $S_{xx}$  and relatively large  $S_{zz}$  (Figure 5a,c) is consistent with the observation reported in ref 6 on larger N–H excursions from their equilibrium orientation in this chain segment.

The irreducible (Wigner scheme) ordering tensor components  $S_0^2 = S_{zz}$  and  $S_2^2 = (2/3)^{1/2}(S_{xx} - S_{yy})$  are shown in Figure 6. The average value of  $S_0^2$  is  $-0.457 \pm 0.017$  for the  $\alpha$ -helix and  $-0.484 \pm 0.002$  for the remaining part of the polypeptide chain.  $S_0^2$  is the same as  $S_{zz}$  which was discussed above. The  $\alpha$ -helix, the strands  $\beta_3$  and  $\beta_4$ , and the loops  $\beta_2/\alpha$ -helix,  $\alpha$ -helix/ $\beta_3$  (except for the residue G41), and  $\beta_3/\beta_4$ , have an average  $S_2^2$  value of  $1.14 \pm 0.03$ . The N-terminal segment of the GB3 backbone comprising the strand  $\beta_1$  and the loop  $\beta_1/\beta_2$  has an average  $S_2^2$  value of  $1.09 \pm 0.02$ . Within the strand  $\beta_2$ ,  $S_2^2$  varies from 1.02 to 1.11. The  $S_2^2$  value of the N–H bond of residue G41 has an outstanding  $S_2^2$  value of 0.918.

In the RDC-based study of ref 6 the local ordering is accounted for empirically by a scaling factor applied to all of the experimental data. This led to the conclusion that “the amplitude of the internal dynamics in GB3 is homogeneous”. Our study shows that  $S_{yy}$  is nearly constant within the  $\alpha$ -helix, whereas  $S_{zz}$  is nearly constant within the  $\beta$ -sheet. Thus, the tensorial perspective of SRLS provides more detailed and better-defined information.

The “flexibility” of the  $\alpha$ -helix detected in ref 7 can be related to the combined effect of local ordering and local diffusion. In this secondary structure element, we find slow local motional correlation times (Figure 4b) and large ordering rhombicity (Figure 6b). Likewise, the RDC-based finding that the N–H bonds of residues K10, L12, A20, V21, and A48 are engaged in large angular excursions<sup>6</sup> is consistent with slow local motion for K10, L12, A20, and V21 (Figure 4b), and weak local ordering around the N–H bond for A48 (Figures 5c and 6a).

Finally, note that the local ordering in the  $\alpha$ -helix is relatively weak but highly rhombic (Figure 6). This finding is consistent with the importance of local ordering rhombicity and the likelihood of this dominant factor being absorbed by  $D_1$  axially.

**3.2.4. Global Diffusion: Moderate Deviations from Spherical Symmetry.** In Section 3.1 we provide evidence that within a good approximation one may use an isotropic global diffusion tensor,  $D_1$  for GB1 and GB3. In general, the deviation of  $D_1$  from spherical symmetry is considered in MF to be a very important factor in the analysis of  $^{15}\text{N}$ –H relaxation from proteins. We have shown previously that this assessment stems from  $D_1$  often absorbing unaccounted for factors, notably unaccounted for asymmetry of the local ordering.<sup>21,22,37</sup> For example, Tables 10 and 11 of ref 21 show that local ordering rhombicity is more important than global diffusion axially. If the local ordering tensor is not allowed to be rhombic while the global diffusion tensor is allowed to be axial (or anisotropic), the unaccounted for rhombicity of the former will be overcome by deviation from spherical symmetry of the latter.<sup>37,45</sup>

We devote this section to an extensive investigation of the effect of  $D_1$  asymmetry on the analysis of  $^{15}\text{N}$  spin relaxation.  $^{15}\text{N}$   $T_1$ ,  $T_2$ , and  $^{15}\text{N}$ – $\{^1\text{H}\}$  NOE are calculated at four magnetic fields using isotropic or anisotropic global diffusion tensor,  $D_1$ , and experimental data from GB3, as an example. For isotropic  $D_1$  we use  $D_{1,\text{iso}} = (5.01 \pm 0.03) \times 10^7 \text{ s}^{-1}$  (which corresponds to  $\tau_m = 3.33 \text{ ns}$ ), and the best-fit parameters obtained with SRLS based fitting of the experimental data denoted “exp” in Table 3. For anisotropic  $D_1$  we use  $D_{1,xx} = (4.13 \pm 0.24) \times 10^7$ ,  $D_{1,yy} = (4.60 \pm 0.18) \times 10^7$  and  $D_{1,zz} = (6.25 \pm 0.34) \times 10^7 \text{ s}^{-1}$  from ref 9; the other input parameters are the same as those used for isotropic  $D_1$ . They appear in Figure 4.

The percent difference between corresponding parameters, defined as  $\sigma(P) = (P(\text{aniso}) - P(\text{iso}))/P(\text{aniso}) \times 100\%$  (where  $P$  denotes  $^{15}\text{N}$   $T_1$ ,  $T_2$ , and  $^{15}\text{N}$ – $\{^1\text{H}\}$  NOE) is shown in



Table 3. Calculated  $^{15}\text{N}$   $T_1$ ,  $T_2$ , and  $^{15}\text{N}\text{--}\{^1\text{H}\}$  NOE Values for Selected Residues of GB3 Using Isotropic or Anisotropic Global Diffusion Tensor,  $D_1^a$ 

residue	magnetic field											
	11.7 T			14.1 T			16.4 T			18.8 T		
	$T_1$ ms	$T_2$ ms	NOE	$T_1$ ms	$T_2$ ms	NOE	$T_1$ ms	$T_2$ ms	NOE	$T_1$ ms	$T_2$ ms	NOE
<b>L5 (<math>\beta_1</math>)</b>												
exp	371.7	203.3	0.620	418.4	192.3	0.700	465.1	190.5	0.740	529.1	180.5	0.760
iso	370.2	200.9	0.633	422.3	197.2	0.694	471.7	189.9	0.735	516.0	180.4	0.765
aniso	369.6	209.9	0.611	417.2	205.9	0.680	461.9	198.5	0.725	502.0	188.7	0.759
$\sigma$ , %	−0.1	4.3	−3.6	−1.2	4.3	−2.1	−2.1	4.3	−1.4	−2.8	4.4	−0.8
<b>V6 (<math>\beta_1</math>)</b>												
exp	383.1	207.9	0.630	423.7	199.2	0.700	497.5	194.6	0.740	537.6	185.9	0.750
iso	381.1	205.9	0.635	436.0	202.1	0.695	488.6	194.8	0.735	536.5	185.1	0.764
aniso	380.7	212.7	0.618	432.0	208.8	0.684	480.9	201.3	0.728	525.4	191.4	0.759
$\sigma$ , %	−0.1	3.2	−2.8	−0.9	3.2	−1.6	−1.6	3.2	−1.0	−2.1	3.3	−0.7
<b>T16 (<math>\beta_2</math>)</b>												
exp	393.7	220.3	0.630	442.5	209.2	0.690	492.6	204.9	0.720	552.5	187.3	0.760
iso	394.2	217.1	0.631	446.8	211.9	0.688	497.1	203.0	0.724	543.1	191.9	0.749
aniso	394.2	225.5	0.611	442.6	220.0	0.675	488.5	210.9	0.716	530.4	199.5	0.745
$\sigma$ , %	0	3.7	−3.3	−1.0	3.7	−1.9	−1.8	3.7	−1.1	−2.4	3.8	−0.5
<b>T17 (<math>\beta_2</math>)</b>												
exp	389.1	220.8	0.640	452.5	210.5	0.690	478.5	192.7	0.740	515.5	182.5	0.780
iso	386.8	212.9	0.640	438.5	207.7	0.698	487.7	199.0	0.735	532.8	188.0	0.761
aniso	387.3	218.9	0.624	435.8	213.4	0.688	481.8	204.5	0.729	523.8	193.4	0.757
$\sigma$ , %	0.1	2.7	−2.6	−0.6	2.7	−1.5	−1.2	2.7	−0.8	−1.7	2.8	−0.5
<b>A29 (<math>\alpha</math>-helix)</b>												
exp	386.1	188.3	0.690	431.0	180.5	0.740	497.5	176.7	0.790	568.2	168.9	0.810
iso	385.4	191.0	0.697	443.5	184.8	0.742	499.0	175.3	0.772	549.9	164.1	0.794
aniso	394.7	179.1	0.715	460.7	172.9	0.752	523.8	163.6	0.778	581.7	152.7	0.796
$\sigma$ , %	2.3	−6.7	2.5	3.7	−6.9	1.3	4.8	−7.2	0.8	5.5	−7.4	0.5
<b>F30 (<math>\alpha</math>-helix)</b>												
exp	359.7	183.8	0.690	411.5	176.4	0.740	452.5	162.9	0.790	490.2	151.3	0.820
iso	351.9	178.0	0.690	405.2	173.5	0.746	456.0	165.8	0.783	502.2	156.3	0.811
aniso	356.9	170.5	0.703	414.7	165.9	0.754	469.7	158.4	0.789	519.7	149.0	0.815
$\sigma$ , %	1.4	−4.4	1.9	2.3	−4.6	1.1	2.9	−4.7	0.8	3.4	−4.9	0.5
<b>K31 (<math>\alpha</math>-helix)</b>												
exp	361.0	178.9	0.710	432.9	169.5	0.760	469.5	161.3	0.780	518.1	148.8	0.830
iso	362.7	175.6	0.711	419.4	170.1	0.760	473.7	161.5	0.794	523.7	151.3	0.819
aniso	372.9	163.6	0.730	438.0	158.0	0.772	500.2	149.7	0.801	557.4	139.8	0.823
$\sigma$ , %	2.8	−7.4	2.6	4.2	−7.6	1.6	5.3	−7.9	0.9	6.1	−8.2	0.5
<b>V39 (loop <math>\alpha</math>-helix/<math>\beta_3</math>)</b>												
exp	396.8	188.7	0.630	438.6	173.6	0.710	495.0	163.4	0.760	540.5	150.8	0.830
iso	380.1	180.9	0.665	440.1	174.9	0.706	497.3	165.9	0.734	549.6	155.1	0.754
aniso	387.0	173.8	0.673	451.8	167.7	0.709	513.5	158.8	0.734	569.9	148.2	0.752
$\sigma$ , %	1.8	−4.1	1.2	2.6	−4.3	0.4	3.2	−4.5	0	3.6	−4.6	−0.3
<b>T44 (<math>\beta_3</math>)</b>												
exp	374.5	207.0	0.630	420.2	198.0	0.710	471.7	194.9	0.750	531.9	179.5	0.770
iso	373.1	203.8	0.640	425.9	200.1	0.703	476.5	192.9	0.745	522.7	183.3	0.775
aniso	372.9	211.4	0.620	421.8	207.5	0.690	468.4	200.1	0.736	510.9	190.3	0.770
$\sigma$ , %	0	2.0	−3.2	−1.0	3.6	−1.9	−1.7	3.6	−1.2	−2.3	3.7	−0.7
<b>T53 (<math>\beta_4</math>)</b>												
exp	374.5	201.2	0.650	429.2	200.4	0.720	454.5	184.8	0.750	495.0	170.1	0.770
iso	364.9	196.7	0.648	417.3	193.4	0.710	466.7	186.7	0.752	510.6	177.6	0.783
aniso	364.4	203.9	0.630	413.0	200.5	0.698	458.6	193.6	0.744	499.1	184.4	0.777
$\sigma$ , %	−0.1	3.5	−2.9	−1.0	3.5	−1.7	−1.8	3.6	−1.1	−2.3	3.7	−0.8

<sup>a</sup>The calculations are designated “iso” and “aniso”, respectively. The best-fit parameters obtained with SRLS-based fitting of the data denoted “exp” with isotropic  $D_1$  were used as input parameters. The difference between relaxation parameters calculated with the “iso” and “aniso” scenarios is given as  $\sigma(P) = [(P(\text{aniso}) - P(\text{iso}))/P(\text{aniso})] \times 100\%$ , where  $P$  denotes  $^{15}\text{N}$   $T_1$ ,  $T_2$ , and  $^{15}\text{N}\text{--}\{^1\text{H}\}$  NOE.

Table 3. For 10 residues residing in different parts of the protein structure, that is, representing a large range of tilt angles between the N–H bond and the axial global diffusion frame, we

find that  $\sigma(P)$  varies from −2.8% to 6.1% for  $T_1$ , from −8.2% to 4.4% for  $T_2$ , and from −3.6 to 2.6% for the NOE. The largest average  $|\sigma(P)|$  value of 4.4% was obtained for  $T_2$ . This is

expected, since for relatively rigid N–H bonds  $R_2 = 1/T_2$  is given largely by  $J^{\text{DD}}(0)$  and  $J^{\text{CC}}(0)$ , which are dominated by the global diffusion.

The average  $|\sigma(P)|$  values are small. In general, they do not exceed the estimated errors in the respective experimental relaxation parameters. The difference between corresponding experimental (“exp”) and back-calculated (“iso”) relaxation parameters does not exceed 4%, in evidence of good statistics. The high quality of the fitting, the evidence and arguments presented in Section 3.1, and the extensive data shown in Table 3 validate the utilization of isotropic  $D_1$  for GB1 and GB3. One may conclude that in general axiality of  $D_1$  on the order of  $D_{1,\parallel}/D_{1,\perp} < 1.4$  may be ignored for globular proteins when the anisotropy of the local spatial restrictions is accounted for, as appropriate.

**3.2.5. The Local Potential.** The best-fit values of the coefficients of the local potential,  $c_0^2$  and  $c_2^2$ , are shown in Figure 4c,d. There is a clear distinction between the values of  $c_0^2$  for the  $\alpha$ -helix (and the N-terminal segment of the loop  $\alpha$ -helix/ $\beta_3$  and the residues A48 and T49) and the remaining part of the polypeptide chain. Because  $X_{\text{OF}}$  is the main ordering axis, the actual potential has a minimum value along  $X_{\text{OF}}$ . To render the potential shape consistent with that scenario, we permute the labels of the OF frame twice counter-clockwise so that  $X_{\text{OF}}$  becomes the new Z-axis. Thus,  $S_{xx} \rightarrow \hat{S}_{zz}$ ,  $S_{yy} \rightarrow \hat{S}_{xx}$  and  $S_{zz} \rightarrow \hat{S}_{yy}$  with the carets representing the permuted OF frame. The corresponding potential coefficients are  $\hat{c}_0^2 = -0.5c_0^2 - (3/2)^{1/2}c_2^2$  and  $\hat{c}_2^2 = 0.5((3/2)^{1/2}c_0^2 - c_2^2)$ .<sup>50</sup>

We show in Figure 7 the potential coefficients  $\hat{c}_0^2$  and  $\hat{c}_2^2$ . The axial potential coefficient,  $\hat{c}_0^2$ , is large throughout the

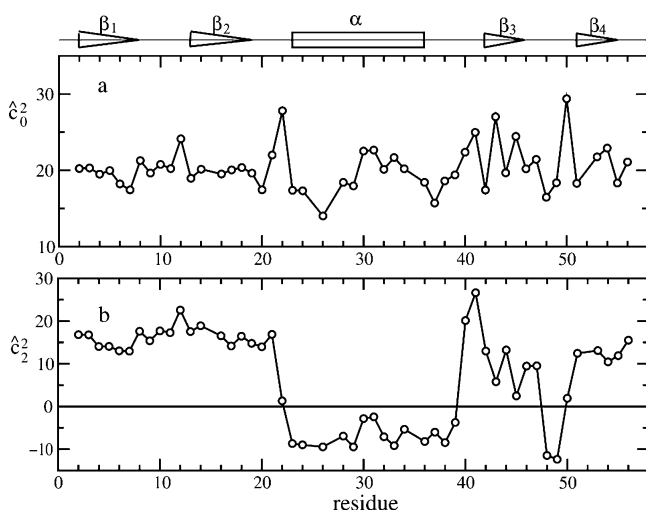


**Figure 7.** Best-fit (a) axial,  $\hat{c}_0^2$ , and (b) rhombic,  $\hat{c}_2^2$ , potential coefficients that correspond to the permuted local ordering frame with  $X_{\text{OF}}$  as main ordering axis. The errors are 15 and 5%, respectively.

polypeptide chain, indicating, as expected, strong local ordering around the  $C_{i-1}^{\alpha} - C_i^{\alpha}$  axis. Its average value,  $\langle \hat{c}_0^2 \rangle$ , equals  $20.3 \pm 2.9$  (in units of  $k_B T$ ). The rhombic potential coefficient,  $\hat{c}_2^2$ , is large and positive for the  $\beta$ -sheet (except for residues A48 and T49), in accordance with  $S_{yy}$  being larger than  $S_{zz}$  (cf. Figure 5). It is large and negative for the  $\alpha$ -helix, in accordance with  $S_{yy}$  being smaller than  $S_{zz}$  (cf. Figure 5). Thus, within the Z–Y local ordering plane, preferential ordering occurs along  $Y_{\text{OF}}$  (the orientation perpendicular to the peptide-bond plane) for the

$\alpha$ -helix and along  $Z_{\text{OF}}$  (the N–H bond orientation) for the  $\beta$ -strands. This strongly supports the assessment that H-bonds stabilize the  $\beta$ -sheet of GB3 structurally.

**3.2.6. Activation Energies for Global and Local Motions.** GB1 and GB3 have similar primary, secondary, and tertiary structures. It is expected that their global and local diffusion properties are also similar. We use the experimental  $^{15}\text{N}$ –H relaxation parameters acquired by Idyaluttin et al.<sup>13</sup> from GB1 in the temperature range of 278–323 K, and magnetic fields of 11.7, 14.1, and 18.8 T, to determine activation energies for the global and local diffusion for these proteins.

**3.2.6.1. Global Motion.** The strategy employed in ref 13 does not provide a global diffusion tensor for GB1. Assuming isotropic global diffusion (see above), we determined from the experimental  $R_2/R_1$  data of ref 13 correlation times for global motion,  $\tau_m$ , of  $5.39 \pm 0.03$ ,  $4.87 \pm 0.23$ ,  $4.16 \pm 0.11$ ,  $3.54 \pm 0.10$ ,  $3.22 \pm 0.07$ ,  $2.92 \pm 0.13$ ,  $2.46 \pm 0.15$ ,  $2.32 \pm 0.18$ , and  $1.98 \pm 0.04$  ns for 278, 283, 288, 293, 298, 303, 308, 313, and 323 K, respectively. The GB1 structure 2GB1 (ref 3), and the program QUADRIC<sup>51</sup> (which is based on a simplified calculation valid for  $D_{1,\parallel}/D_{1,\perp} < 2.0$ )<sup>52</sup> were used. The  $\tau_m$  values listed above represent averages over calculations carried out by us separately for magnetic fields of 11.7, 14.1, and 18.8 T.

The straight red line in Figure 8 shows  $\ln(D_1)$  (where  $D_1 = 1/(6\tau_m)$ ) as a function of  $1/T$ . Clearly, the Arrhenius relation is

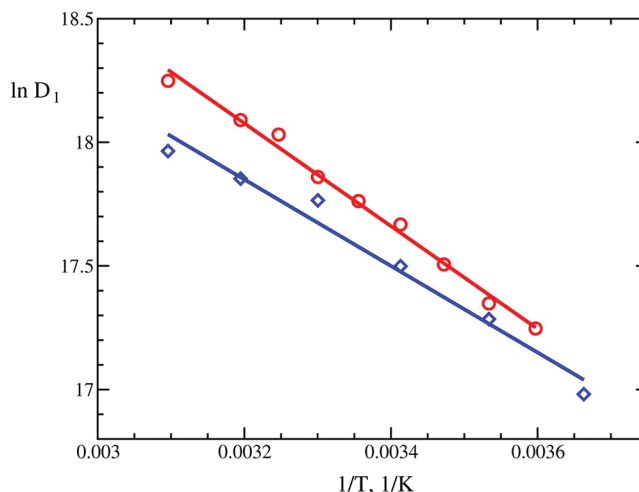


**Figure 8.** Arrhenius plot for the global diffusion of GB1, with the rates ( $D_1$ ), calculated using the data of ref 13 (red; see text) and the data of ref 12 (blue).

fulfilled. The slope of this line yields an activation energy for global motion given by  $E_a(\text{global}) = (17.3 \pm 0.6)$  kJ/mol. In a previous study,<sup>53</sup> we detected significant differences between the activation energies for global diffusion of compact proteins, and proteins that exhibit internal domain motion. The activation energy for the self-diffusion of water is  $(15.4 \pm 0.3)$  kJ/mol. Compact proteins have generally larger activation energies due to the hydration layer attached to the protein surface via electrostatic interactions.<sup>53</sup> Proteins that exhibit domain motion have generally smaller activation energies, often similar to that of water, because domain motion disrupts these interactions.<sup>53</sup> The value of  $(17.3 \pm 0.6)$  kJ/mol obtained for GB1 is relatively large, in accordance with its compact structure.

We also show in Figure 8  $\ln(D_1)$  as a function of  $1/T$  obtained using the  $^{15}\text{N}$ –H relaxation data from GB1 of Seewald et al.,<sup>12</sup> acquired in the temperature range of 273–323 K, and a

magnetic field of 14.1 T (blue line). In this case, the functional dependence is not linear; the activation energy obtained is  $(14.6 \pm 1.1)$  kJ/mol. This value is substantially smaller than the value obtained using the data of Idyatullin et al.<sup>13</sup> The nonlinearity of the  $\ln(D_1)$  versus  $1/T$  plot might be associated with protein aggregation (the protein concentration used in ref 12 is 2.7 mM as compared to 1.6 mM in ref 13). This is an interesting observation to be further explored.

**3.2.6.2. Local Motion.** Using the  $\tau_m$  values depicted above, we applied the “rhombic potential” SRLS scheme to the experimental data of ref 13. From the best-fit values of the local motional rate,  $D_2$ , we derived activation energies,  $E_a(\text{local})$ , based on the Arrhenius relation. Table 4 shows the results

**Table 4. Activation Energies,  $E_a(\text{local})$ , for Local N–H Motion in GB1 Derived from the Best-Fit Values of  $D_2$  Obtained with the “Rhombic Potential” SRLS Scheme Applied to the Experimental Data of ref 13<sup>a</sup>**

secondary structure element	residue	$E_a(\text{local})$ , kJ/mol	$\ln A$
strand $\beta_1$	K4	$40.9 \pm 1.0$	$37.0 \pm 0.4$
strand $\beta_1$	L5	$36.6 \pm 2.4$	$35.2 \pm 1.0$
strand $\beta_1$	I6	$37.6 \pm 3.1$	$35.7 \pm 1.3$
loop $\beta_1/\beta_2$	L12	$16.9 \pm 1.3$	$27.3 \pm 0.5$
strand $\beta_2$	E15	$34.5 \pm 1.2$	$34.5 \pm 0.5$
strand $\beta_2$	T17	$59.3 \pm 3.9$	$44.8 \pm 1.6$
strand $\beta_2$	T18	$36.4 \pm 1.4$	$35.1 \pm 0.6$
loop $\beta_2/\alpha\text{-helix}$	D22	$20.1 \pm 0.6$	$27.8 \pm 0.3$
$\alpha\text{-helix}$	A26	$18.9 \pm 0.4$	$27.4 \pm 0.1$
$\alpha\text{-helix}$	K28	$28.7 \pm 1.7$	$31.0 \pm 0.7$
$\alpha\text{-helix}$	K31	$24.4 \pm 2.2$	$29.3 \pm 0.9$
$\alpha\text{-helix}$	A34	$20.9 \pm 1.1$	$28.0 \pm 0.4$
loop $\alpha\text{-helix}/\beta_3$	G41	$19.8 \pm 0.8$	$27.1 \pm 0.3$
strand $\beta_3$	W43	$48.9 \pm 3.6$	$40.2 \pm 0.9$
strand $\beta_3$	T44	$46.6 \pm 2.4$	$39.4 \pm 1.0$
strand $\beta_3$	Y45	$43.1 \pm 3.2$	$38.0 \pm 1.3$
loop $\beta_3/\beta_4$	A48	$28.6 \pm 1.4$	$31.4 \pm 0.6$
strand $\beta_4$	T53	$40.5 \pm 2.1$	$36.5 \pm 0.8$
strand $\beta_4$	V54	$48.4 \pm 0.6$	$40.4 \pm 0.3$
strand $\beta_4$	T55	$47.0 \pm 1.7$	$39.6 \pm 0.7$

<sup>a</sup>The global diffusion rate,  $D_1$ , was determined as outlined in the text. The pre-exponential factor in the Arrhenius relation is given as  $\ln A$ .

obtained for the representative residues K4, L5, and I6 of the strand  $\beta_1$ ; L12 of the loop  $\beta_1/\beta_2$ ; E15, T17, and T18 of the strand  $\beta_2$ ; D22 of the loop  $\beta_2/\alpha\text{-helix}$ ; A26, K28, K31, and A34 of the  $\alpha\text{-helix}$ ; G41 of the loop  $\alpha\text{-helix}/\beta_3$ ; W43, T44, and Y45 of the strand  $\beta_3$ ; and T53, V54, and T55 of the strand  $\beta_4$ .

The average  $E_a(\text{local})$  values for the strands  $\beta_1$ ,  $\beta_2$ ,  $\beta_3$ , and  $\beta_4$  are  $38.4 \pm 2.3$ ,  $43.4 \pm 3.9$ ,  $46.2 \pm 2.9$ , and  $45.3 \pm 4.2$  kJ/mol, respectively. The overall average is  $43.3 \pm 7.1$  kJ/mol. For the  $\alpha\text{-helix}$   $\langle E_a(\text{local}) \rangle = 23.2 \pm 4.3$  kJ/mol, which is substantially smaller than the average activation energy for the  $\beta$ -strands. The smallest  $\langle E_a(\text{local}) \rangle$  values were obtained for the loops. They vary from 16.9 kJ/mol for the loop  $\beta_1/\beta_2$  to 28.6 kJ/mol for the loop  $\beta_3/\beta_4$ . For the loops  $\beta_1/\beta_2$ ,  $\beta_2/\alpha\text{-helix}$ , and  $\alpha\text{-helix}/\beta_3$  that experience slower motion (Figure 4a), the activation energy equals, on average,  $18.9 \pm 1.8$  kJ/mol. This value exceeds insignificantly the activation energy for the global diffusion of GB1,  $17.3 \pm 0.6$  kJ/mol. The activation energy for the loop  $\beta_3/\beta_4$  is comparable to that for the  $\alpha\text{-helix}$ .

The relatively large activation energies for the  $\beta$ -strands as compared to the  $\alpha\text{-helix}$  might be associated with a well-structured

four-stranded antiparallel-parallel-antiparallel  $\beta$ -sheet reinforced by a network of inter-related H-bonds. There is evidence in the literature for a network of H-bonds that creates a standing wave across the  $\beta$ -sheet of GB3.<sup>49</sup> Structural stiffening implied by arrays of cooperative H-bonds is suggested in a recent quantum chemical study.<sup>54</sup> Our results are consistent with these findings.

Unlike the  $\beta$ -sheet, the  $\alpha$ -helix of GB1 comprises independent H-bonds. This implies reduced activation energy for local N–H motion. Further reduction occurs for the loops, where H-bonds are rare or nonexistent.

It is of interest to compare the activation energies for local motion in GB1 with those of other proteins. We found previously<sup>34</sup> that the activation energies for internal motion of the domains AMPbd and LID of AKeco are  $63.8 \pm 7.0$  and  $53.0 \pm 9.1$  kJ/mol, respectively. The activation energy for the P-loop of AKeco is  $16.5 \pm 6.4$  kJ/mol. That the activation energy for the motions of the AMPbd and LID domains of AKeco is larger than  $E_a(\text{local})$  for the N–H bonds of GB1 is likely to be associated with collective local motions in the former case as compared to individual N–H motions in the latter case. The relatively slowly moving loops  $\beta_1/\beta_2$ ,  $\beta_2/\alpha\text{-helix}$ , and  $\alpha\text{-helix}/\beta_3$  of GB1, and the P-loop of AKeco have similar  $E_a(\text{local})$  value. Further studies are required to establish whether relatively small activation energies are characteristic of loops in proteins.

To our knowledge, this is the first derivation of physically well-defined activation energies for local N–H motion in proteins. It will be of interest to compare the SRLS-derived values of  $E_a(\text{local})$  with their MD-derived counterparts.

**3.3. MF Analysis – refs 9, 10, and 13.**  $^{15}\text{N}$   $T_1$ ,  $T_2$ , and  $^{15}\text{N}\text{--}\{^1\text{H}\}$  NOE relaxation parameters from GB3 acquired at 14.1 T and 297 K were analyzed with the standard MF method, taking the global diffusion axially symmetric.<sup>9</sup> This analysis used primarily model 2, where  $S^2$  and  $\tau_e$  are allowed to vary. The local motion is described by the squared generalized order parameter,  $S^2$ . On average,  $S^2$  is relatively large for the  $\alpha\text{-helix}$ , smaller for the strands  $\beta_1$  and  $\beta_4$ , and further reduced for the strands  $\beta_2$  and  $\beta_3$ . Small  $S^2$  values have been obtained for the C-termini of the loops  $\beta_1/\beta_2$  and  $\alpha\text{-helix}/\beta_3$ , and the middle part of the loop  $\beta_3/\beta_4$  (Figure 3 of ref 9, empty circles).

The study reported in ref 9 was extended in ref 10 by also acquiring  $^{15}\text{N}\text{--}\text{H}$  relaxation parameters at 9.4, 11.7, 16.4, and 18.8 T. The combined multifield data set could not be analyzed with good statistics using the strategy used in ref 9. It could be analyzed allowing the  $^{15}\text{N}$  CSA tensor to vary.<sup>10</sup> There is controversy in the field with regard to the extent to which the  $^{15}\text{N}$  CSA tensor varies from site to site.<sup>10,46,55–59</sup> Several groups carried out quantum chemical calculations.<sup>60–62</sup> The respective results partly disagree and are often inconsistent with corresponding solid-state NMR results.<sup>63</sup> Since variations in  $^{15}\text{N}$  CSA are not limited by physical constraints, it is relatively easy to achieve good statistics in the data-fitting process.

As pointed out above, the parameters called “activation energy” in ref 13 relate to empirical decay constants that parametrize the spectral density rather than principal values of a diffusion tensor.

**3.4. Formal Comparison between SRLS and MF Results.** The SRLS results consist of well-defined parameters.  $D_2$  is the principal value of the local diffusion tensor,  $S_0^2$  and  $S_2^2$  are the principal values of the local ordering tensor, and  $\beta_D \equiv \beta_{\text{OF-DF}}$  is the polar angle in the Wigner rotation from the local ordering frame, OF, to the magnetic dipolar frame, DF.



MF yields the squared generalized order parameter,  $S^2$ , which is a composite. Since this parameter is the same in any coordinate frame, let us calculate it in the principal axis system (PAS) of the local ordering tensor.

$S^2$  is defined as<sup>14</sup>

$$S^2 = \frac{4}{5} \pi \sum_{m=0,\pm 1,\pm 2} |\langle Y_{2,m} \rangle \langle Y_{2,-m} \rangle|$$

$$= \sum_{m=0,\pm 1,\pm 2} |\langle D_{0,m}^2 \rangle \langle D_{0,-m}^2 \rangle| \quad (8)$$

In the PAS of the local ordering tensor this yields:

$$S^2 = \langle D_{0,0}^2 \rangle^2 + 2\{\text{Re}\langle D_{0,2}^2 \rangle\}^2 \quad (9)$$

Since

$$S_0^2 = \langle D_0^2 \rangle \text{ and } S_2^2 = \langle D_{0,2}^2 + D_{0,-2}^2 \rangle = 2\{\text{Re}\langle D_{0,2}^2 \rangle\} \quad (10)$$

one obtains:

$$S^2 = (S_0^2)^2 + \frac{1}{2}(S_2^2)^2 \quad (11)$$

We calculated  $S^2$  using eq 11 and the  $S_0^2$  and  $S_2^2$  values given in Figure 6; our results are shown in Figure 9a. The empty

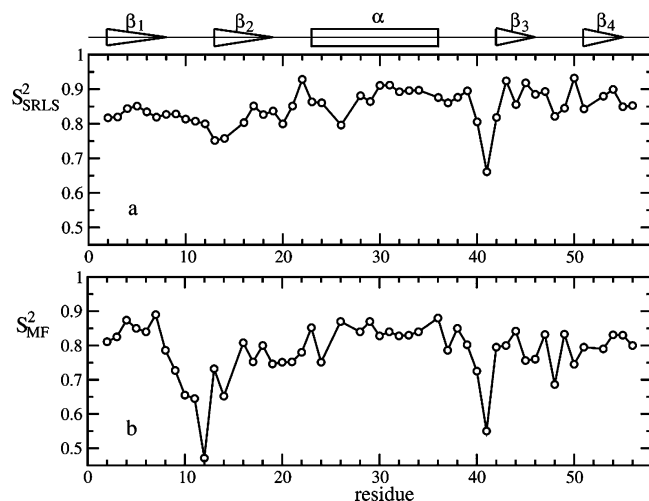


**Figure 9.** (a)  $S_{\text{SRLS}}^2$  calculated according to eq 11 using  $S_0^2$  and  $S_2^2$  data shown in Figure 6. (b)  $S_{\text{MF}}^2$  determined in ref 10 using combined data acquired at 9.4, 11.7, 14.1, 16.4, and 18.8 T, and 297 K.

circles in Figure 9b, reproduced from ref 9, show  $S^2$  as given by MF. The agreement is poor because  $S^2$  derived with MF has absorbed unaccounted for factors.

#### 4. CONCLUSIONS

We applied the SRLS approach to  $^{15}\text{N}$  spin relaxation from GB3 and GB1. In agreement with previous SRLS applications to other proteins, we find that physically insightful results are contingent upon accounting properly for the asymmetry of the spatial restriction at the site of the motion of the N–H bond. Only in this case it is possible to analyze combined multifield data from GB1 and GB3 using a standard fitting scheme with constant magnetic tensors and determine physically well-defined descriptors of restricted local motions, including their activation energies. In particular, the site-specific eigenvalues and the

principal axis systems of the rhombic local ordering tensors, and the principal value of isotropic local diffusion tensors provide new physical insights. It has been ascertained that the main local ordering axis at N–H sites in proteins is directed along  $\text{C}_{i-1}^\alpha - \text{C}_i^\alpha$ . The conspicuous experimental distinction between the  $\alpha$ -helix and the remaining part of the GB3 backbone has been shown to represent a combination of structural (ordering), kinetic (diffusion-related), and geometric properties characteristic of the  $\alpha$ -helix, rather than axial global diffusion. For the first time, activation energies for local N–H motion in proteins have been derived from eigenvalues of diffusion tensors, which is the standard approach for small molecules. For GB1 they decrease from the  $\beta$ -sheet through the  $\alpha$ -helix to the loops.

#### AUTHOR INFORMATION

##### Corresponding Author

\*E-mail: shapiro@nmrsg4.lsbu.ac.il (Y.E.S.), meirove@biu.ac.il (E.M.).

##### Notes

The authors declare no competing financial interest.

#### ACKNOWLEDGMENTS

This work was supported by the Israel Science Foundation (Grant No. 347/07 to E.M.), the Binational Science Foundation (Grant No. 2006050 to E.M. and Jack H. Freed), the German-Israeli Science Foundation for Scientific Research and Development (Grant No. 928-190.0/2006 to E.M. and Christian Griesinger of Max Planck Institute, Göttingen, Germany), and the Damadian Center for Magnetic Resonance at Bar-Ilan University, Israel.

#### REFERENCES

- (1) Derrick, J. O.; Wigley, D. B. *J. Mol. Biol.* **1994**, *243*, 906–918.
- (2) Ulmer, T. S.; Ramirez, B. E.; Delaglio, F.; Bax, A. *J. Am. Chem. Soc.* **2003**, *125*, 9179–9191.
- (3) Gronenborn, A. M.; Filpula, D. R.; Essig, N. Z.; Achari, A.; Whitlow, M.; Wingfield, P. T.; Clore, G. M. *Science* **1991**, *253*, 657–661.
- (4) Konradi, R.; Billeter, M.; Wüthrich, K. *J. Mol. Graph.* **1996**, *14*, 51–55.
- (5) Shen, Y.; Vernon, R.; Baker, D.; Bax, A. *J. Biomol. NMR* **2009**, *43*, 63–78.
- (6) Yao, L.; Vogeli, B.; Torchia, D. A.; Bax, A. *J. Phys. Chem. B* **2008**, *112*, 6045–6056.
- (7) Clore, G. M.; Schwieters, C. D. *J. Mol. Biol.* **2006**, *355*, 879–886.
- (8) Li, T.; Jing, Q.; Yao, L. *J. Phys. Chem. B* **2011**, *115*, 3488–3495.
- (9) Hall, J. B.; Fushman, D. *J. Biomol. NMR* **2003**, *27*, 261–275.
- (10) Hall, J. B.; Fushman, D. *J. Am. Chem. Soc.* **2006**, *128*, 7855–7870.
- (11) Barchi, J. J. Jr.; Grasberger, B.; Gronenborn, A. M.; Clore, M. G. *Protein Sci.* **1994**, *3*, 15–21.
- (12) Seewald, M. J.; Pichumani, K.; Stowell, C.; Tibbals, B. V.; Regan, L.; Stone, M. J. *Protein Sci.* **2000**, *9*, 1177–1193.
- (13) Idyatullin, D.; Nesmelova, I.; Daragan, V. A.; Mayo, K. H. *J. Mol. Biol.* **2003**, *325*, 149–162.
- (14) Lipari, G.; Szabo, A. *J. Am. Chem. Soc.* **1982**, *104*, 4546–4559.
- (15) Lipari, G.; Szabo, A. *J. Am. Chem. Soc.* **1982**, *104*, 4559–4570.
- (16) Clore, G. M.; Szabo, A.; Bax, A.; Kay, L. E.; Driscoll, P. C.; Gronenborn, A. M. *J. Am. Chem. Soc.* **1990**, *112*, 4989–4991.
- (17) Polimeno, A.; Freed, J. H. *Adv. Chem. Phys.* **1993**, *83*, 89–206.
- (18) Polimeno, A.; Freed, J. H. *J. Phys. Chem.* **1995**, *99*, 10995–11006.
- (19) Liang, Z.; Freed, J. H. *J. Phys. Chem. B* **1999**, *103*, 6384–6396.
- (20) Tugarinov, V.; Liang, Z.; Shapiro, Yu. E.; Freed, J. H.; Meirovitch, E. *J. Am. Chem. Soc.* **2001**, *123*, 3055–3063.

- (21) Meirovitch, E.; Shapiro, Yu. E.; Polimeno, A.; Freed, J. H. *J. Phys. Chem. A* **2006**, *110*, 8366–8396.
- (22) Meirovitch, E.; Shapiro, Yu. E.; Polimeno, A.; Freed, J. H. *Prog. NMR Spectrosc.* **2010**, *56*, 360–405.
- (23) E. Meirovitch, E.; Polimeno, A.; Freed, J. H. Protein Dynamics by NMR Spin Relaxation: The Slowly Relaxing Local Structure Perspective. In *Encyclopedia of Magnetic Resonance*; Harris, R. K.; Wasylishen, R. E., Eds.; John Wiley: Chichester, 2011. DOI: 10.1002/9780470034590.emrstm1243.
- (24) Nordio, P. L.; Busolin, P. *J. Chem. Phys.* **1971**, *55*, 5485–5490.
- (25) Polnaszek, C. F.; Bruno, G. V.; Freed, J. H. *J. Chem. Phys.* **1973**, *58*, 3185–3199.
- (26) Polnaszek, C. F.; Freed, J. H. *J. Phys. Chem.* **1975**, *79*, 2283–2306.
- (27) *NMR of Liquid Crystals*; Emsley, J. W., Ed.; Reidel Publishers, Dordrecht, 1985.
- (28) *The Molecular Dynamics of Liquid Crystals*; Luckhurst, G. R.; Veracini, C. A., Eds.; Kluwer Academic Publishers: The Netherlands, 1994.
- (29) Meirovitch, E.; Zerbetto, M.; Polimeno, A.; Freed, J. H. *J. Phys. Chem. B* **2011**, *115*, 143–157.
- (30) Meirovitch, E.; Shapiro, Yu. E.; Zerbetto, M.; Polimeno, A. *J. Phys. Chem. B* **2012**, *116*, 886–894.
- (31) Shapiro, Yu. E.; Kahana, E.; Tugarinov, V.; Liang, Z.; Freed, J. H.; Meirovitch, E. *Biochemistry* **2002**, *41*, 6271–6281.
- (32) Tugarinov, V.; Shapiro, Yu. E.; Liang, Z.; Freed, J. H.; Meirovitch, E. *J. Mol. Biol.* **2002**, *315*, 155–170.
- (33) Shapiro, Yu. E.; Meirovitch, E. *J. Phys. Chem. B* **2006**, *110*, 11519–11524.
- (34) Shapiro, Yu. E.; Kahana, E.; Meirovitch, E. *J. Phys. Chem. B* **2009**, *113*, 12050–12060.
- (35) Bremi, T.; Brüschweiler, R. *J. Am. Chem. Soc.* **1997**, *119*, 6672–6673.
- (36) Lienin, S. F.; Bremi, T.; Brutscher, B.; Brüschweiler, R.; Ernst, R. R. *J. Am. Chem. Soc.* **1998**, *120*, 9870–9879.
- (37) Zerbetto, M.; Polimeno, A.; Meirovitch, E. *J. Phys. Chem. B* **2009**, *113*, 13613–13625.
- (38) Abragam, A. *Principles of Nuclear Magnetism*; Oxford University Press (Clarendon): London, 1961.
- (39) Peng, J. W.; Wagner, G. In *Methods in Enzymology*; James, T. L.; Oppenheimer, N. J., Eds.; Academic Press, New York, 1994; Vol. 239, pp 563–595.
- (40) Cavanagh, J.; Fairbrother, W. J.; Palmer, A. G., III; Skelton, N. J., *Protein NMR Spectroscopy: Principles and Applications*, San-Diego: Academic Press, 1996.
- (41) Tjandra, N.; Szabo, A.; Bax, A. *J. Am. Chem. Soc.* **1996**, *118*, 6986–6991.
- (42) Kroenke, C. D.; Loria, J. P.; Lee, L. K.; Rance, M.; Palmer, A. G. III *J. Am. Chem. Soc.* **1998**, *120*, 7905–7915.
- (43) Brink, D. M.; Satchler, G. R. *Angular Momentum*; Clarendon Press: Oxford, 1968.
- (44) Freed, J. H. *J. Chem. Phys.* **1977**, *66*, 4183–4199.
- (45) Meirovitch, E.; Shapiro, Yu. E.; Tugarinov, V.; Liang, Z.; Freed, J. H. *J. Phys. Chem. B* **2003**, *107*, 9883–9897.
- (46) Kroenke, C. D.; Rance, M.; Palmer, A. G. *J. Am. Chem. Soc.* **1999**, *121*, 10119–10125.
- (47) Mandel, A. M.; Akke, M.; Palmer, A. G. III *J. Mol. Biol.* **1995**, *246*, 144–163.
- (48) Fushman, D.; Cahill, S.; Cowburn, D. *J. Mol. Biol.* **1997**, *266*, 173–194.
- (49) Bouvignies, G.; Bernado, P.; Meier, S.; Cho, K.; Grzesiek, S.; Brüschweiler, R.; Blackledge, M. *Proc. Natl. Acad. Sci. U.S.A.* **2005**, *102*, 13885–13890.
- (50) Barnes, J. P.; Freed, J. H. *Biophys. J.* **1998**, *75*, 2532–2546.
- (51) Lee, L. K.; Rance, M.; Chazin, W. J.; Palmer, A. G. *J. Biomol. NMR* **1997**, *9*, 287–298.
- (52) Brüschweiler, R.; Liao, X.; Wright, P. E. *Science* **1995**, *268*, 886–889.
- (53) Shapiro, Yu. E.; Meirovitch, E. *J. Phys. Chem. B* **2009**, *113*, 7003–7011.
- (54) Novikov, A. N.; Shapiro, Yu. E. *J. Phys. Chem. A* **2011**, *116*, 546–559.
- (55) Fushman, D.; Tjandra, N.; Cowburn, D. *J. Am. Chem. Soc.* **1998**, *120*, 10947–10952.
- (56) Köver, K.; Batta, G. *J. Magn. Reson.* **2001**, *150*, 137–146.
- (57) Damberg, P.; Jarvet, J.; Graslund, A. *J. Am. Chem. Soc.* **2005**, *127*, 1995–2005.
- (58) Loth, K.; Pelupessy, P.; Bodenhausen, G. *J. Am. Chem. Soc.* **2005**, *127*, 6062–6068.
- (59) Yao, L.; Grishaev, A.; Cornilescu, G.; Bax, A. *J. Am. Chem. Soc.* **2010**, *132*, 4295–4309.
- (60) Cai, L.; Kosov, D. S.; Fushman, D. *J. Biomol. NMR* **2011**, *50*, 35–42.
- (61) Tang, S.; Case, D. A. *J. Biomol. NMR* **2011**, *51*, 313–318.
- (62) Frank, A.; Onila, I.; Moller, H. M.; Exner, T. *Proteins* **2011**, *79*, 2189–2202.
- (63) Wylie, B. J.; Rienstra, C. *J. Chem. Phys.* **2008**, *128*, 052207/23.